



HAL
open science

Origin of dissolved gas (CO₂, O₂, N₂, alkanes) in pore waters of a clay formation in the critical zone (Tégulines Clay, France)

Catherine Lerouge, Mathieu Debure, Benoît Henry, Ana-Maria Fernandez, Michaela Blessing, Eric Proust, Benoît Madé, Jean-Charles Robinet

► To cite this version:

Catherine Lerouge, Mathieu Debure, Benoît Henry, Ana-Maria Fernandez, Michaela Blessing, et al. Origin of dissolved gas (CO₂, O₂, N₂, alkanes) in pore waters of a clay formation in the critical zone (Tégulines Clay, France). *Applied Geochemistry*, 2020, 116, pp.104573. 10.1016/j.apgeochem.2020.104573 . hal-02913643

HAL Id: hal-02913643

<https://brgm.hal.science/hal-02913643>

Submitted on 5 Dec 2022

HAL is a multi-disciplinary open access archive for the deposit and dissemination of scientific research documents, whether they are published or not. The documents may come from teaching and research institutions in France or abroad, or from public or private research centers.

L'archive ouverte pluridisciplinaire **HAL**, est destinée au dépôt et à la diffusion de documents scientifiques de niveau recherche, publiés ou non, émanant des établissements d'enseignement et de recherche français ou étrangers, des laboratoires publics ou privés.

1 Title: Origin of dissolved gas (CO₂, O₂, N₂, alkanes) in pore waters of a clay formation in the
2 critical zone (Tégulines Clay, France)

3

4 Catherine Lerouge¹, Mathieu Debure¹, Benoit Henry¹, Ana-Maria Fernandez², Michaela
5 Blessing¹, Eric Proust¹, Benoit Madé³, Jean-Charles Robinet³

6 1. BRGM, 3 Avenue Claude Guillemin, 45060 Orléans cédex 2

7 2. CIEMAT, Departamento de Medio Ambiente, 28040 Madrid, Spain

8 3. ANDRA, 1-7 rue Jean-Monnet, 92298 Châtenay-Malabry Cedex, France

9 Abstract

10

11 Understanding weathering processes in clay formations is an issue of primary importance for
12 the preservation of our natural environment. Reactive-transport modeling used to simulate
13 weathering of clay formations has indicated that reactive gases (CO₂ and O₂) are major
14 parameters in controlling weathering processes.

15 The Lower Cretaceous Tégulines marine-clay formation outcropping in the area of Brienne-
16 le-Chateau (north-eastern France) has been investigated in the context of a sub-surface
17 waste repository. We developed gas monitoring (CO₂, O₂, N₂, alkanes) of core samples from
18 two boreholes that entirely crosscut the Tégulines Clay formation, to define the
19 consequences of weathering and oxidation processes on gases dissolved in pore waters. We
20 discuss amounts of gas and the carbon isotopic composition of CO₂ in terms of pore-water
21 chemistry including dissolved-inorganic carbon (DIC) and alkalinity, mineral reactivity,
22 organic-matter degradation and oxygen diffusion. Degassing of samples conditioned under
23 He atmosphere provided evidence of very high CO₂ production in the soil (0-30 cm), and high
24 CO₂ degassing associated with a high oxygen level in the first 2-10 m of the clay. The CO₂
25 degassing increase observed in weathered clay relative to preserved clay resulted from
26 calcite dissolution due to pyrite oxidation and organic matter degradation. The δ¹³C of CO₂
27 indicates that organic matter degradation was a major source of CO₂ at shallow depths and
28 down to 10-12 m, which is the maximum depth at which we observed fossil roots. Then the
29 CO₂ degassing decreased down to a constant value in preserved clay, where the carbonate
30 system and the mineral assemblage control dissolved carbonates in pore waters. The profile
31 of the δ¹³C_{CO2} also provides evidence of progressive CO₂ diffusion of organic origin from the
32 underlying Greensands aquifer in the lower part of Tégulines Clay up to ~ 40 m in the
33 AUB230 borehole.

34 As a first step toward understanding interactions between Tégulines Clay and near surface
35 waters or water at the Greensands interface, we developed a reactive-transport model to
36 simulate in one dimension weathering processes under ambient temperature, constrained by
37 geochemical reactions in soil (organic matter degradation) and in the clay (pyrite oxidation
38 and calcite dissolution), exchange, DIC and pore water chemistry. The simulation was
39 carried out for 10 kyrs, assuming that weathering and soil formation began after the last
40 glacial maximum. The DIC profile cannot be simulated without considering evaporation
41 processes in agreement with the isotopic data. This type of approach combining a complete
42 field dataset (reactive-gas concentrations, δ¹³C of CO₂, major-ion concentrations, δ¹⁸O and
43 δD of pore waters) and reactive-transport modeling is necessary for better understanding of
44 chemical weathering processes in the critical zone.

45

46 Keywords: chemical weathering, critical zone, pore waters, dissolved gas, carbon stable

47 isotopes, Tégulines Clay, reactive transport modeling

48

49 **1. Introduction**

50 The critical zone (CZ) extends from vegetation to groundwater and is a system that combines
51 chemical, biological, physical, and geological processes supporting life all together (Brantley
52 et al., 2007; Brantley et al., 2013; Sullivan et al., 2016; White et al., 2015). Among the
53 various lithologies, marine-clay formations represent ~25 % of the continental surface. They
54 are of peculiar interest due to their low permeability, complex fluid and gas transfers (slow
55 vertical diffusion/lateral transfer), buffer capacity associated with carbonate minerals, and
56 early diagenetic mineral assemblages. These are largely controlled by microbial activity and
57 are consequently redox sensitive (Duffy et al., 2014; Lerouge et al., 2014; Lerouge et al.,
58 2011). Interactions between marine-reduced clay formation, atmosphere and hydrosphere
59 induce mineral, chemical, pore water, petrophysical and mechanical changes in the clay
60 formation (Brantley et al., 2013; Lerouge et al., 2018; Soulet et al., 2018a; Sullivan et al.,
61 2016; Yesavage et al., 2012 and references therein). Most of these interactions and changes
62 are driven by biological activity, including macro- and micro-organisms, and vegetation. Clay-
63 rock reactivity includes pyrite oxidation and sulfur state/pH changes, carbonate
64 dissolution/alkalinity/DIC changes, organic matter degradation/DOC changes (Dideriksen et
65 al., 2007; Drake et al., 2009; Duffy et al., 2014; Lerouge et al., 2018; Mazurek et al., 1996;
66 Soulet et al., 2018a), and changes in other redox proxies (Tostevin et al., 2016; Yu et al.,
67 2017). The progression of the weathering and oxidizing fronts is controlled by 1) the meteoric
68 water influx rate, 2) oxidation reaction kinetics (pyrite oxidation, organic matter degradation),
69 and 3) oxygen flux (Bolton et al., 2006; Brantley et al., 2013; Li et al., 2017). While numerous
70 data are available on mineral reactions and pore water chemistry in the critical zone, little are
71 available on gas transfer through the vadose zone and are essentially obtained by reactive-
72 transport modeling (Hasenmueller et al., 2017; Heidari et al., 2017).

73
74 Among scientific research on radioactive-waste disposal in deep geological clay formations,
75 a core degassing methodology has been developed to monitor degassing in reduced-marine
76 claystone conditioned in gas containers under helium just after sampling (Girard et al., 2005).
77 The numerous degassing experiments carried out on cores of reduced-marine claystone
78 (Callovian-Oxfordian Clay, Opalinus Clay, Toarcian shales of Tournemire) provided evidence
79 of CO₂ and alkane steady state being attained after few months, and a relatively
80 homogeneous range of CO₂ partial pressures (P_{CO_2}) between 6 and 12 mbar (Gaucher et al.,
81 2010; Lerouge et al., 2015; Wersin et al., 2016). The $\delta^{13}C$ of the degassed CO₂ and of calcite
82 separated from the claystone confirmed the thermodynamic equilibrium between carbonate
83 solution species and calcite (Gaucher et al., 2010; Girard et al., 2005; Lerouge et al., 2015).

84

85 In this paper, we applied and developed the core degassing methodology to the Tégulines
86 Clay of the Lower Cretaceous age that outcrops in the north-eastern part of the Paris Basin
87 in France. For a decade, Tégulines Clay was investigated in the context of surface repository
88 for low-level radioactive waste (Debure et al., 2018; Duffy et al., 2014; Lerouge et al., 2018).
89 Chemical, mineral, and petrophysical characterization of core samples from two drilling
90 campaigns in 2013 and 2015 provided evidence of weathering and oxidation processes
91 down to ~20 m depth (Lerouge et al., 2018). Due to the significant mineral and pore-water
92 changes including the perturbation of the carbonate system, it is of major interest to
93 investigate the consequences of weathering and oxidation processes on core degassing in
94 Tégulines Clay. We monitored CO₂, O₂, N₂ and alkanes degassed by core samples from
95 three boreholes crosscutting the clay down to the Greensands aquifer, providing dissolved
96 gas data through the critical zone. Amounts of gas, carbon isotopic composition of CO₂ and
97 reactive transport modeling are discussed in terms of pore water chemistry, CO₂ origins, gas
98 transfer, and key parameters for the understanding of weathering processes in the critical
99 zone.

100

101 **2. Geological setting and sampling**

102 **2.1. Geological setting**

103 The Gault clay formation in the Aube department in the eastern part of the Paris Basin
104 consists of siliciclastic shales deposited in an open marine environment from Middle to Upper
105 Albian (Lower Cretaceous) on the Greensands formation (Amédéo et al., 2014). The
106 stratotype of the Gault Clay defined in the Aube department consists of the Argiles Tégulines
107 de Courcelles (82 m) overlain by the Marnes de Brienne (43 m). At -23 Ma (Early Miocene),
108 the Paris Basin was eroded and became almost similar to the present day. Nowadays the
109 Gault Clay formation outcrops as a 8-10 km large and 80-km long band of terranes oriented
110 NE-SW through the Aube department (Figure 1a).

111 In the area we studied east of Brienne Le Chateau, Gault Clay is only represented by
112 Tégulines Clay. The claystones consisted of the dominant clay fraction (47-72 %) associated
113 with a quartz-feldspar silty fraction (28-43 %) and a carbonate fraction (0-22%) (Lerouge et
114 al., 2018). Weathering of Tégulines Clay induced petrophysical, mineralogical and chemical
115 changes (Lerouge et al., 2018).

116 **2.2. Sampling and rock description**

117 Samples were collected on three boreholes: AUB1010, AUB230 and AUB240, and a 5-meter
118 deep pit (TPH1-1) (Figure 1b). The AUB1010 borehole, drilled in May 2015, crosscuts less
119 than 1.9 m of surficial formations/ weathered clay that were lost during the drilling, and ~32 m
120 of clay before attaining the Greensands. Seventeen core samples came from the Tégulines
121 Clay. The AUB230 borehole, drilled in December 2017 near the TPH1-1 pit, crosscuts ~5 m
122 of surficial formations and ~63 m of Tégulines Clay before attaining the Greensands. Eight
123 samples came from surficial formations dug in TPH1-1 pit and 28 core samples from
124 Tégulines Clay. The AUB240 borehole was drilled in May 2018. About 12 m of Brienne marls
125 overlie ~70 m of Tégulines Clay and protect them from weathering (Figure 1b). Twelve core
126 samples came from the Brienne marls and 18 core samples from Tégulines Clay. All of these
127 core samples were water-saturated.

128 The mineralogy and weathering profile of the AUB1010 borehole are detailed in Lerouge et
129 al. (2018). The TPH1-1 pit and the AUB230 borehole were drilled in a cultivated cornfield in
130 December 2017. The 0-0.3 m was a brownish sandy loam soil containing ~1.5 wt % of
131 organic carbon. In the TPH1-1 pit, the following 0.3-5 m were ochrous sandy loam formed of
132 61-70 % quartz-feldspar sandy fraction and 21-32 % of clay fraction that were crosscut by a
133 grayish network associated with local black roots. Some detrital disseminated coarse quartz
134 grains (up to 400 μm) are characteristic of these surficial formations. Surficial formations in
135 the AUB230 borehole, ~10 meters from the TPH1-1 pit, were very similar but the bottom part
136 was poorer in coarse detrital quartz grains, and looked like in situ dismantled Tégulines Clay.
137 The organic matter content of the 0-5 m zone was lower than 0.2 wt.%. The mineralogy of
138 the clay in the AUB230 borehole was quite similar to the AUB1010 borehole, taking into
139 account that the 34 meters of the clay in the AUB1010 borehole corresponded to the last 34
140 meters of the clay overlying Greensands aquifer (Lerouge et al., 2018) (Figure 2). The
141 organic matter content of Tégulines Clay is $\sim 0.5 \pm 0.1$ wt.% (Duffy et al., 2014). The bottom
142 of the clay formation is characterized by the highest clay content (70-72 wt %), 27-29 wt % of
143 quartz – feldspar silty fraction and no carbonate. The overlying ~ 9-12 m corresponds to the
144 clay-quartz rich unit (UAQ) and is characterized by high quartz – feldspar silty content
145 (AUB1010: 41-43 wt %; AUB230: 39-44 wt %) and low carbonate contents of 0-9 %. The
146 overlying ~20 m crosscut in the AUB1010 borehole and ~35 m in the AUB230 borehole
147 corresponded to the clay rich unit (UA unit) and were characterized by the highest clay
148 content (AUB1010: 54-66 wt %; AUB230: 50-53 wt %), 4-8 % of carbonates and lower
149 quartz-feldspar silty content (32-41 wt %). The overlying ~20-25 m crosscut only in the
150 AUB230 borehole belonged to the carbonate-clay rich unit (UAC) with the highest calcite
151 contents (16-27 wt %) and the lowest quartz – feldspar silty contents (20-31 wt %).

152 The oxidation profile developed in the clay from the AUB230 borehole was also very similar
153 to that of the AUB1010 borehole, although the thickness in the two boreholes was very
154 different. The top of the clay attained at 3.5-5 m below the ground surface consists of a
155 plastic entirely oxidized claystone (57 % of clay and 42 % of quartz-feldspar), which
156 progressively becomes greenish with a brown network associated with roots. Pyrite nodules
157 and framboids entirely broke down into gypsum associated with goethite. Carbonates are not
158 detected by XRD but were still observed in thin sections (Figure 3). The 5-11 m were plastic,
159 yellowish green, and highly reactive; all the Fe-bearing minerals, including pyrite, glauconite
160 were partially oxidized. Calcite gave evidence of partial dissolution, while gypsum and
161 goethite precipitated (Figure 3). Down to a depth of 20-25 m, Tégulines Clay is plastic, green
162 with rare yellowish aggregates of glauconite that attest to tiny oxidation (Debure et al., 2018;
163 Lerouge et al., 2018). Below 20-25 m, the reduced clay is dark green, nonplastic,
164 nonfractured and unoxidized. Diagenetic assemblage including framboidal pyrite, calcite,
165 glauconite and francolite supports reducing conditions.
166

167 **3. Methods**

168 **3.1. Squeezing and pore water chemistry**

169 Pore waters were extracted from clay samples by squeezing (Fernández et al., 2014), but
170 using a modified method for collecting the squeezed pore waters under anoxic conditions.
171 This method had already been applied to clay core samples from the AUB1010 borehole
172 (Lerouge et al., 2018). The core sample mass was measured before and after squeezing.
173 The initial core sample masses ranged between 300 and 500 g. Extractions were carried out
174 at pressures ranging between 5 and 60 MPa (Table 1) over 9 days. Approximately 20 mL of
175 pore water was collected. Two successive pressures were applied to some samples to favor
176 pore water extraction, as indicated in Table 1.

177 **3.2. Core degassing protocol**

178 **3.2.1. Conditioning on the field**

179 Core samples were immediately conditioned on the field after leaving the core sampler in
180 order to minimize contact with atmosphere and to preserve in situ conditions of the clay-
181 rocks, in particular the redox state. The first centimeters around the core were cut to avoid
182 contamination of the clay by drill muds. The core samples were conditioned in glass jars of

183 0.5, 1 or 1.5 L under a He pressure of 600-700 10^{-3} bar after three short cycles of pumping
184 and filling of He up to a pressure of 1.5 bar. The vacuum obtained with the pump
185 corresponded to about 20-30 10^{-3} bar. The pumping time was short to avoid clayrock
186 desaturation. The three successive cycles of pumping and He fillings decreased the oxygen
187 content in the gas phase ($<5 \cdot 10^{-7}$ moles of O_2). The samples were systematically weighed
188 and ranged between 900 and 1000 g in a 1.5 L glass jar. The weight was proportionally
189 adapted for other glass jars.

190 3.2.2. Gas monitoring

191 Glass jars were stored in a room at an almost constant temperature ($\sim 20^\circ\text{C}$), and regularly
192 monitored for total gas pressure (P_{total} expressed in bar) and concentrations of different gas
193 species (CO_2 , alkanes, oxygen and nitrogen) on a Varian star 3400 CX gas chromatograph
194 over several months (at least 2 months). Oxygen and nitrogen gases were systematically
195 measured to test the gas-tightness of the glass jars. Concentrations of gas species (X_{gas}
196 $_{\text{species}}$) are given in volume percent. The uncertainty on the concentrations of CO_2 , alkanes, O_2
197 and N_2 in the gas phase was 3 %. The detection limits for gas concentrations were 0.001 %
198 for CO_2 , O_2 and N_2 , and 0.0002 % for alkanes. The uncertainty on the total pressure
199 measured in the chromatograph was $3 \cdot 10^{-3}$ bar. Data are firstly expressed in partial pressure
200 of gas species ($P_{\text{gas species}}$) using Equation 1:

$$201 \quad P_{\text{gas species}} = \frac{X_{\text{gas species}}}{100} \times P_{\text{total}} \quad (\text{eq 1})$$

202 To establish the degassing duration necessary for a steady state and improve the technique,
203 the seventeen clay core samples from the AUB1010 borehole of the 2015 drilling campaign
204 were regularly monitored for CO_2 for more than 200 days in the laboratory. The P_{CO_2} attained
205 a steady state at about 60 days of degassing in all the gas-tight glass jars (Figure 4a). In five
206 glass jars where P_{total} , P_{O_2} and P_{N_2} increased slowly toward atmospheric values, providing
207 evidence of micro-leaks, the P_{CO_2} went on to increase slowly (Figure 4b). Two monitorings
208 carried out on two aliquots of AUB1010-13.45 m showed that the P_{CO_2} measured in a leaking
209 glass jar was higher than that measured in a gas-tight jar (Figure 4b). In this study, the
210 values of P_{CO_2} measured at 60 days in gas-tight jars were considered as representative of the
211 P_{CO_2} of the gas/solid/pore water steady state.

212 3.2.3. Carbon isotopic composition of CO_2

213 At the final stage of core degassing, an aliquot of gas of each sample was transferred into
214 He-flushed Labco®-vials. The stable carbon isotopic composition of CO_2 ($\delta^{13}\text{C}_{\text{CO}_2}$) was

215 analyzed with a continuous flow Thermo Finnigan Delta^{plus} XP isotope ratio mass
216 spectrometer equipped with a GasBench II (Thermo Finnigan) for gas preparation and
217 introduction. Isotopic compositions are reported in δ units relative to international standards,
218 defined by: $\delta = (R_{\text{Sample}}/R_{\text{Standard}} - 1) \times 1000 \text{ ‰}$. where R is the measured isotopic ratio in the
219 sample and in the standard: Vienna Standard Mean Ocean Water (V-SMOW) for oxygen,
220 Vienna Pee Dee Belemnite (V-PDB) for carbon. Internal reproducibility was $\pm 0.2 \text{ ‰}$ for
221 oxygen and carbon; accuracy for $\delta^{13}\text{C}$ measurements with respect to V-PDB standard is
222 better than $\pm 0.5 \text{ ‰}$.

223 **3.2.4. Successive core-degassing**

224 Core degassing classically analyzes present-day dissolved gas. We now apply successive
225 degassing stages to a same core sample, to define the origin of the gas, and the processes
226 that controlled their production. Reproducible concentrations of a gas species during
227 successive degassing would indicate that the rock controls the processes of gas formation.
228 Decreasing concentrations of a gas species during successive degassing would suggest that
229 the gas species is present as a finite stock in the claystone.

230 At the end of the first monitoring and the sampling of the gas aliquot for the $\delta^{13}\text{C}_{\text{CO}_2}$
231 measurement, all the gas was pumped out of the glass jar, and the core sample was re-
232 conditioned under a He pressure of 600-700 10^{-3} bar. The glass jar was again regularly
233 monitored for total gas pressure (P_{total}) and concentrations of different gas species (CO_2 ,
234 alkanes, oxygen and nitrogen), according to the § 3.2.2. The reconditioning was applied two
235 times to clay core samples from the AUB1010 and AUB230 boreholes.

236 **3.3. Calculation of the concentrations of dissolved gas in pore** 237 **waters**

238 With the knowledge of all the parameters of the core degassing experiment, it is possible to
239 estimate the initial concentrations of dissolved gas in pore waters (referred to as
240 $[\text{gas species}]_0$) from the final measured partial pressures of gas ($P_{\text{gas species}}$). The
241 experiment is a closed system in which the core sample degasses in an atmosphere of inert
242 gas until obtaining steady state between gas, pore waters and solid (Figure 5). In the initial
243 system (0), core sample is water-saturated and the gas phase is only He. In the final system
244 (f), gas species present in the gas phase are considered at equilibrium with gas dissolved in
245 pore waters.

246 **3.3.1. Oxygen and nitrogen**

247 For gases such as oxygen and nitrogen, which are not controlled by the rock, the gas content
248 in the rock represents a gas stock, which distributes between the gas phase (*gas*) and pore
249 waters (*aq*) during the experiment. Consequently, for such gas species, it is possible to write
250 the conservation equation of the species in the (gas + pore waters) system, as follows:

251
$$n_{\text{gas species}}(aq)_0 = n_{\text{gas species}}(gas)_f + n_{\text{gas species}}(aq)_f \quad (\text{eq. 2})$$

252 where $n_{\text{gas species}}(gas)_f$ is the number of moles of the gas species at the end of the
253 experiment, and $n_{\text{gas species}}(aq)_0$ and $n_{\text{gas species}}(aq)_f$ are the number of moles of the gas
254 species dissolved in pore waters of the core sample at the beginning and at the end of the
255 experiment, respectively.

256 The term $n_{\text{gas species}}(aq)$ depends on the sample mass (M), on the water content of the
257 sample (W %) and on the concentration of the gas species dissolved in pore waters
258 ($[\text{gas species}]$) as follows:

259
$$n_{\text{gas species}}(aq) = \frac{M}{100} \times \frac{W}{1000} \times [\text{gas species}] \quad (\text{eq. 3})$$

260 By replacing $n_{\text{gas species}}(aq)$ in equation 2 with the above expression, $[\text{gas species}]_0$ can be
261 expressed in function of $n_{\text{gas species}}(gas)_f$, M , W and $[\text{gas species}]_f$ as follows:

262
$$[\text{Gas species}]_0 = n_{\text{gas species}}(gas)_f / \left(\frac{M}{100} \times \frac{W}{1000} \right) + [\text{gas species}]_f \quad (\text{eq. 4})$$

263 The term $n_{\text{gas species}}(gas)_f$ can be deduced from the ideal gas law applied to the partial
264 pressure of the gas species $P_{\text{gas species}}$, and measured in the volume of gas (V_G) of the glass
265 jar:

266
$$n_{\text{gas species}}(gas)_f = P_{\text{gas species}} \times \frac{V_G}{R \times T} \quad (\text{eq. 5})$$

267

268 The $[\text{gas species}]_f$ can be deduced from the Henry's law as follows:

269
$$[\text{gas species}]_f = \frac{P_{\text{gas species}}}{K_{\text{H}}(\text{gas species})} \quad (\text{eq. 6})$$

270 Replacing $n_{\text{gas species}}(gas)_f$ and $[\text{gas species}]_f$ in Equation 4 with the above expressions,
271 $[\text{Gas species}]_0$ can finally be expressed as a function of $P_{\text{gas species}}$, V_G , M , W , and
272 $K_{\text{H}}(\text{gas species})$, which are known parameters:

273 $[\text{Gas species}]_0 = P_{\text{gas species}} \times \left\{ \left(\frac{V_G}{R \times T} \right) / \left(\frac{M}{100} \times \frac{W}{1000} \right) + \frac{1}{K_{H(\text{gas species})}} \right\}$ (eq 7)

274

275 Nitrogen gas may be considered as an inert gas diffusing through Tégulines Clay. We
 276 consequently apply Equation 7 directly to estimate concentrations of dissolved N₂ in
 277 Tégulines pore waters. At 25°C, $K_{H(\text{N}_2)}$ is 1639.34 (Schaap et al., 2001), and the term
 278 $1/K_{H(\text{N}_2)}$ is negligible.

279 Oxygen gas is a reactive gas diffusing through Tégulines Clay. For this reason, the
 280 concentrations of dissolved O₂ in Tégulines pore waters that may be calculated using
 281 Equation 7 need to be taken with caution, and probably represent minimum values. $K_{H(\text{O}_2)}$ is
 282 769.23 at 25°C (Schaap et al., 2001), and $1/K_{H(\text{O}_2)}$ is negligible, as is the case for nitrogen
 283 gas.

284

285 3.3.2. Dissolved inorganic carbon (DIC)

286 Contrary to O₂ and N₂ gas, for which gas pressure is directly related to dissolved gas
 287 concentration by the Henry law, the CO₂ partial pressure is related to dissolved CO₂ by the
 288 Henry law, but total dissolved inorganic carbon is distributed among three species CO₂(aq),
 289 HCO₃⁻ and CO₃²⁻. Consequently, calculations need to take into account all the carbonate
 290 species dissolved in pore waters as the total dissolved carbonate content (DIC) is defined by:

291 $\text{DIC} = [\text{CO}_2(\text{aq})] + [\text{HCO}_3^-] + [\text{CO}_3^{2-}]$ (eq 8)

292 At equilibrium, [HCO₃⁻] and [CO₃²⁻] can be expressed in term of [CO₂(aq)], K_1 , K_2 and [H⁺],
 293 K_1 being the reaction constant for CO₂(aq) = H⁺ + HCO₃⁻ and K_2 being the reaction constant
 294 for HCO₃⁻ = H⁺ + CO₃²⁻ (Giffaut et al., 2014):

295 $\text{DIC} = [\text{CO}_2(\text{aq})] \times (1 + K_1 \times [\text{H}^+] + K_1 \times K_2 \times [\text{H}^+]^2)$ (eq 9)

296 Taking into account all the carbonate species dissolved in pore waters, the conservative
 297 Equation 2 can be applied to the total amount of moles of carbonates dissolved in pore
 298 waters ($n_{\text{DIC}}(\text{aq})$) and CO₂ gas ($n_{\text{CO}_2}(\text{gas})$) during experiments, as follows:

299 $n_{\text{DIC}}(\text{aq})_0 = n_{\text{CO}_2}(\text{gas})_f + n_{\text{DIC}}(\text{aq})_f$ (eq 10)

300 By replacing $n_{\text{DIC}}(\text{aq})$ by their expressions given in equation 3, total dissolved inorganic
 301 carbon content DIC₀ can be expressed in function of $n_{\text{gas species}}(\text{gas})_f$, M, W and
 302 [gas species]_f:

303 $DIC_0 = n_{CO_2}(gas)_f / \left(\frac{M}{100} \times \frac{W}{1000} \right) + DIC_f$ (eq 11)

304 According to the ideal gas law, $n_{CO_2}(gas)_f = P_{CO_2} \times \frac{V_G}{R \times T}$

305 According to equation 9 applied to final state of the experiment,

306 $DIC_f = [CO_2(aq)]_f \times (1 + K_1 \times [H^+] + K_1 \times K_2 \times [H^+]^2)$

307 $DIC_f = P_{CO_2} / K_{H(CO_2)} \times (1 + K_1 \times [H^+] + K_1 \times K_2 \times [H^+]^2)$, with $[CO_2(aq)]_f = P_{CO_2} / K_{H(CO_2)}$

308 Replacing $n_{CO_2}(gas)_f$ and DIC_f in Equation 11 by the above expressions, DIC_0 can finally be
 309 expressed as a function of P_{CO_2} , V_G , M , W , and $K_{H(CO_2)}$, which are known parameters:

310
$$DIC_0 = P_{CO_2} \times \left\{ \left(\frac{V_G}{R \times T} \right) / \left(\frac{M}{100} \times \frac{W}{1000} \right) + \frac{(1 + K_1 \times [H^+] + K_1 \times K_2 \times [H^+]^2)}{K_{H(CO_2)}} \right\}$$
 (eq 11)

311 For CO_2 , contrary to O_2 and N_2 , the term $\frac{(1 + K_1 \times [H^+] + K_1 \times K_2 \times [H^+]^2)}{K_{H(CO_2)}}$ is low but cannot be

312 neglected. $[H^+]$ is deduced from the pH values of pore waters extracted by squeezing. The
 313 equilibrium constants pK_1 and pK_2 are 6.37 and 10.33 at 25°C (Giffaut et al., 2014).

314 4. Results

315 4.1. Pore-water chemistry

316 Pore waters of four samples of surficial formation from the TPH1-1 pit and of eleven clay
 317 core samples from the AUB230 borehole were extracted by squeezing. Natural ground
 318 waters from the TPH1-1 were also collected at 5.4 meters deep. The chemistry of the pore
 319 waters was given in Table 1.

320 The pore waters extracted from surficial formations and natural ground waters at 5.4 m in the
 321 TPH1-1 pit have neutral pH values of ~7.2-7.4, and low alkalinities of 0.57 meq/L PW. It is
 322 noteworthy that pore waters extracted by squeezing and natural pore waters in surficial
 323 formations have consistent chemical compositions. The clay's pore waters have pH values
 324 ranging from 7.4 to 8.2, and alkalinity ranging from 1.2 to 9.9 meq/L. Pore waters in samples
 325 from the lower part of the clay formation are characterized by the lowest alkalinity values and
 326 may be classified as Ca-sulfate type waters. Pore waters in weathered samples of the upper
 327 part of the clay formation are characterized by increasing alkalinity and evolve to Ca-Mg-
 328 sulfate type waters toward the surface.

329 **4.2. Gas monitoring**

330 We applied a core-degassing protocol to the eight samples of surficial formation from the 5-
331 meter deep TPH1-1 pit, the twelve samples of Brienne marls from the AUB240 borehole, and
332 the sixty-three clay core samples from the three AUB240 (18 samples), AUB230 (28
333 samples) and AUB1010 (17 samples) boreholes. We applied two other successive core
334 degassing procedures on the clay core samples from the AUB230 borehole and the
335 AUB1010 borehole, in order to define the process of gas formation. All the gas
336 measurements were expressed as concentrations of dissolved gas in mmol/L of pore water
337 (supplementary data; Figure 6). The P_{CO_2} were also given for comparison with literature data
338 (supplementary data).

339 **4.2.1. Gas monitoring of reduced Tégulines Clay: AUB240 reference borehole**

340 About twelve meters of Brienne marls overly Tégulines Clay in borehole AUB240 and protect
341 them from weathering. Core degassing of overlying Brienne marls have CO_2 concentrations
342 ranging between 1.2 and 4.3 mmol/L PW. The highest values are measured in the upper part
343 of the Brienne marls in contact with alluvium. The O_2 concentrations vary a lot with values up
344 to 0.39 mmol/L PW, and N_2 concentrations range between 0.7 and 7.7 mmol/L PW.

345 The CO_2 , O_2 and N_2 profiles of reduced Tégulines Clay with depth are almost flat. A
346 reference-average CO_2 concentration calculated between the top of the clay at 20 m and the
347 bottom at 90 m is 1.5 ± 0.5 mmol/L PW. The O_2 concentrations were generally below the
348 detection limit except for four samples, whereas the average N_2 concentration was 1.8 ± 1.0
349 mmol/L PW. The CH_4 concentrations ranged between $1.15 \cdot 10^{-3}$ and $4.3 \cdot 10^{-3}$ mmol/L PW. The
350 highest values were measured in the middle of the formation.

351 **4.2.2. Gas monitoring of weathered Tégulines Clay: AUB1010 and AUB230** 352 boreholes

353 *AUB230 borehole*

354 The 5-meter deep TPH1-1 pit and the AUB230 borehole crosscut ~5 m of surficial formations
355 consisting of soil and sandy loam, and ~63 m of weathered Tégulines Clay before attaining
356 the Greensands. The soil sample (TPH1-1 0-30 cm) directly in contact with the atmosphere
357 degassed a lot of CO_2 (11.5 mmol CO_2 /kg of soil), and a significant amount of CH_4 ($1.9 \cdot 10^{-1}$
358 mmol/L PW). The N_2 concentration was high (10.6 mmol/L PW), whereas the O_2
359 concentration was very low (0.04 mmol/LPW). Samples of underlying surficial formations
360 down to 5 m degassed less CO_2 than soil (1.4-2.7 mmol/L PW). The O_2 and N_2 concentrations

361 varied a lot with values up to 2.1 and 11.7 mmol/L PW, respectively. Methane was not
362 detected. The CO₂, O₂ and N₂ profiles of weathered Tégulines Clay with depth are curvilinear
363 (Figure 6). The O₂ concentrations reached up to 0.9 mmol/L PW in the 5-10 m zone and
364 were close to the detection limit below 10 m down to 68 m. The N₂ profile was almost flat with
365 values ranging between 1.4 and 4.7 mmol/L; increased N₂ concentrations was however
366 observed at ~25 m (up to 6.9 mmol/L PW). The CO₂ concentrations significantly increased up
367 to 8.5 mmol/L PW in the 5-15 m zone, in relation with the increase of the O₂ concentrations.
368 Below ~20 m, the CO₂ concentrations ranged between 0.5 and 3.3 mmol/L PW, with an
369 average value of 1.6 ± 0.9 mmol/L PW. The CH₄ concentrations ranged between $4.1 \cdot 10^{-4}$ and
370 $\sim 3.5 \cdot 10^{-3}$ mmol/L PW with the highest value measured in the middle of the formation.

371 *AUB1010 borehole*

372 Tégulines Clay is very close to the surface in the AUB1010 borehole. The CO₂, O₂ and N₂
373 profiles of the weathered clay with depth are also curvilinear (Figure 6). The O₂
374 concentrations reached up to 1.8 mmol/L PW in the 1.9-10 m zone and were close to the
375 detection limit below 10 m down to 34 m, whereas the N₂ concentrations varied a lot, ranging
376 between 2.3 and 14.2 mmol/L PW. The CO₂ concentrations significantly increased up to
377 8.6 mmol/L PW in the 1.9-15 m zone, in relation with the increase of the O₂ concentrations.
378 Below ~20 m, the CO₂ concentrations ranged between 1.2 and 2.8 mmol/L PW, with an
379 average value of 1.7 ± 0.8 mmol/L. The CH₄ concentrations were lower than $9.6 \cdot 10^{-4}$ mmol/L
380 PW, except a value of $1.5 \cdot 10^{-3}$ mmol/L PW at interface with Greensands.

381 *Second and third gas degassing*

382 The CO₂ profiles of the second degassing of core samples from boreholes AUB1010 and
383 AUB230 have the same shape as the CO₂ profiles from the first degassing (Figure 7).
384 However, the CO₂ values measured in the upper part (< 15 m) were lower than that of the
385 first degassing at the same depth (Figure 7). The CO₂ profile of the third degassing was quite
386 flat, with an average CO₂ concentration of 1.4 ± 0.7 mmol/L PW for the AUB1010 borehole
387 and of 1.6 ± 0.7 mmol/L PW for the AUB230 borehole.

388 Oxygen, nitrogen and methane concentrations measured in gas during the second and third
389 degassings were near or below the detection limit of the technique.

390 **4.3. Carbon isotopic composition of CO₂**

391 The $\delta^{13}\text{C}_{\text{CO}_2}$ largely ranged between -25.5 and -7.7 ‰ PDB. The profiles of $\delta^{13}\text{C}_{\text{CO}_2}$ with
392 depth were different in the three boreholes (Figure 8). The $\delta^{13}\text{C}_{\text{CO}_2}$ profile of reduced
393 Tégulines Clay from the AUB240 borehole with depth was almost flat, with values ranging

394 between -12.0 and -7.9 ‰ PDB. The highest values were measured at the top in contact with
395 Brienne marls. The $\delta^{13}\text{C}_{\text{CO}_2}$ of Brienne marls are in the same range as Tégulines Clay.

396 The profiles of $\delta^{13}\text{C}_{\text{CO}_2}$ of the AUB1010 and AUB230 boreholes with depth are curvilinear.
397 The $\delta^{13}\text{C}_{\text{CO}_2}$ of the clay from the AUB230 and AUB1010 boreholes ranged between -19.5 and
398 -10.5 ‰ PDB, and between -19.8 and -12.5 ‰ PDB, respectively. The highest values were
399 measured at ~20-22 m for the AUB1010 borehole (-12.9 to -12.5 ‰ PDB), and between 15
400 and 40 m for the AUB230 borehole (-11.8 to -10.3 ‰ PDB). The lowest values were
401 measured toward the top and the bottom of the formation.

402 The surficial formations overlying the clay in the AUB230 borehole had the lowest values: -
403 25.5 ‰ VPDB for the soil sample (TPH1-1 0-30 cm) in contact with atmosphere, and -21 ‰
404 VPDB for underlying sandy loam.

405 **5. Discussion**

406 **5.1. Dissolved gas contents of reduced Téguline Clay pore waters** 407 **– Comparison with other reduced-marine clays**

408 The most representative, well-preserved reduced Tégulines Clay from the AUB240 borehole
409 between 20 and 90 m deep is characterized by O_2 concentrations below the detection limit
410 and an average P_{CO_2} of $4.1 \pm 0.9 \cdot 10^{-3}$ bar. These results are in the range of P_{CO_2} compiled
411 by Aarão Reis and Brantley (2019) for sedimentary confined aquifers (1 to 100 mbar at
412 25 °C), and of P_{CO_2} values of other marine reduced formations (Gaucher et al., 2010;
413 Gaucher et al., 2009; Lerouge et al., 2015; Tremosa et al., 2012; Wersin et al., 2016). The
414 P_{CO_2} profile with depth is almost flat. This can be a good indication of internal control of this
415 parameter by the mineralogy as its nature is constant throughout the formation.

416 The highest $\delta^{13}\text{C}_{\text{CO}_2}$ (-10.4 to -7.9 ‰) are consistent with $\delta^{13}\text{C}_{\text{CO}_2}$ calculated at equilibrium
417 with calcite in Tégulines Clay, where the $\delta^{13}\text{C}$ ranges between 0.4 and 2.9 ‰ (Lerouge et al.,
418 2018), and carbon isotopic fractionation between calcite and $\text{CO}_2(\text{g})$ of 10.5 ‰ at 20°C
419 (Deines et al., 1974; Mook et al., 1974). They also agree well with values measured in other
420 reduced clay formations, and confirm that degassed CO_2 is controlled by carbonates in the
421 mineral assemblage and not by degradation of organic matter or diffusion of gas coming from
422 other geological formations (Gaucher et al., 2006; Gaucher et al., 2010; Girard et al., 2005;
423 Tremosa et al., 2012).

424 **5.2. Influence of weathering on chemistry and dissolved gas**
425 **contents of Téguline Clay pore waters**

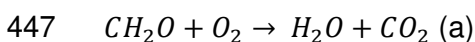
426 Present-day pore waters from Tégulines Clay outcrops have a complex history resulting from
427 their past interactions with external waters coming from overlying Cretaceous chalk, and from
428 their current interactions with percolating meteoric waters and ground waters of the
429 underlying Greensands aquifer. Tégulines Clay is a marine-clay formation that originally
430 evolved in reducing conditions. After 23 Ma of erosion in the Paris Basin, present-day
431 Tégulines clay outcrops or is overlaid by soils and a few meters of surficial formations in the
432 studied area. The bottom of the Tégulines Clay is in contact with the Greensands aquifer,
433 whose water recharge is located less than 10 km southeast.

434 Below we discuss the nature of the external fluids and modifications to the chemistry and
435 dissolved gas (O₂, N₂ and CO₂) concentrations in Tégulines Clay pore waters through the
436 weathering profile.

437 **5.2.1. Surficial fluids through soil and surficial formations**

438 At surface and down to the top of the clay (example of the AUB230 borehole), pore waters
439 are infiltrating meteoric waters, which interact with mineral assemblage in carbonate-free soil
440 and surficial formations. These waters analyzed by squeezing and natural ground waters
441 collected in the pit at ~5.4 m were much-diluted Ca – HCO₃⁻ type waters.

442 The pore water at 0-30 cm shows the highest alkalinity: ~ 1.4 meq/L. The δ¹³C_{CO2} of soil (-
443 25.5 ‰) indicates that the CO₂ derived from organic matter degradation. During the
444 monitoring of soil degassing, the CO₂ concentration rapidly increased, whereas O₂
445 concentration was low (supplementary data). These data indicate that CO₂ results from the
446 degradation of organic matter, according to the respiration reaction (a):



448 Between 0.3 and 5 m, the DIC of surficial formations were less than 0.9 meq/L. The
449 significant DIC difference between soil and surficial formations can be interpreted in different
450 ways:

- 451 1) CO₂ was produced internally by soil and surficial formations, and DIC differences
452 were due to lower organic matter content in surficial formation (0.2 wt.%) than in soil
453 (1.5 wt.% in soil);

- 454 2) CO₂ was produced internally by soil and surficial formations, and DIC differences
455 were due to lower oxygen support in surficial pore waters than in soil; the diffusion
456 rate of dissolved oxygen was four times lower than that of oxygen gas (Bolton et al.,
457 2006);
458 3) CO₂ produced by organic matter degradation migrated into surficial formation.

459 The presence of abnormal high O₂ and N₂ concentrations in surficial formations (higher than
460 dissolved gas solubility) indicates the presence of trapped atmosphere bubbles. That also
461 strongly suggests that organic matter is not degraded much in the surficial formation. The flat
462 CO₂ profile in the surficial formation would rather indicate advective transport of CO₂
463 produced by soil through surficial formation toward Tégulines Clay.

464

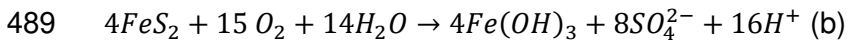
465 **5.2.2. Weathered Tégulines Clay**

466 Pore waters at the top of the Tégulines Clay have a significantly higher ionic strength than
467 pore waters infiltrated from surficial formations and well-preserved, reduced Tégulines Clay
468 pore waters, due to higher alkalinity, and calcium, chloride and sulfate contents. Core
469 degassing also provided evidence of the highest DIC (up to ~9 mmol/L PW), and dissolved
470 O₂ and N₂ concentrations. Some O₂ and N₂ concentration values were higher than gas
471 solubility; that could be due to uncertainties on the water content, desaturation of the sample,
472 or air bubbles trapped by the core samples.

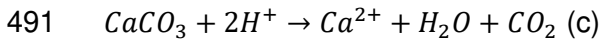
473 The highest chemical changes were observed from the top of the formation down to ~10 m,
474 corresponding to the highly reactive transition zone (AUB1010: Lerouge et al. (2018);
475 AUB230: this study). These changes in pore water chemistry have already been described in
476 other case studies (Brantley et al., 2013; Hendry and Wassenaar, 2000; Jin and Brantley,
477 2011; Tuttle and Breit, 2009; Tuttle et al., 2009) and predicted by reactive-transport
478 modelling of weathering in clay aquitard (Heidari et al., 2017; Jin et al., 2010; Kim and Lee,
479 2009).

480 Chemical variations in the pore water, including high alkalinity and DIC, result from
481 interactions between oxygenated surficial waters and mineral assemblage of the reduced
482 clay. The O₂ concentrations recorded in this zone attest to the presence of O₂ that drives
483 oxidative weathering of pyrite, organic matter and other Fe²⁺ bearing minerals including clay
484 minerals (illite, illite-smectite mixed layers, chlorite, glauconite), carbonates (ankerite) and
485 magnetite, (Brantley et al., 2013; Duffy et al., 2014; Lerouge et al., 2018). The oxidation of
486 pyrite in the presence of water is a source of protons according to reaction (b) that

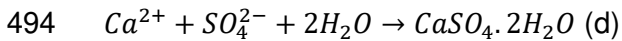
487 contributes to carbonate dissolution and DIC increase (Lebedeva et al., 2007; Torres et al.,
488 2014):



490 The increase of protons induces calcite dissolution according to reaction (c):



492 Iron hydroxides and gypsum are secondary minerals formed from reactions (b) and (d),
493 respectively:



495

496 Below 10-11 m down to ~15-18 m, the DIC, dissolved O₂ and N₂ concentrations, and cation
497 and anion concentrations rapidly decreased to reach a relatively homogeneous reduced clay
498 composition. The O₂ concentration became close or below the detection limit in agreement
499 with reducing conditions.

500 At the bottom of the Tégulines Clay in contact with Greensands, pore waters had a
501 significantly lower ionic strength than pore waters in preserved clay, providing exchanges
502 between Tégulines clay and the Greensands aquifer. The low ionic strength of pore waters
503 was related to slightly lower DIC than reference Tégulines Clay. Claystone does not show
504 any evidence of weathering, but calcite is absent.

505 **5.2.3. Origin of dissolved inorganic carbon in weathered Tégulines Clay**

506 The major reactions increasing the DIC in weathered Tégulines Clay are the dissolution of
507 carbonates present in the claystone and the degradation of organic matter from external and
508 internal sources. The wider $\delta^{13}C_{CO_2}$ range (-19.8 to -10.5 ‰) of the weathered clay than for
509 reduced clay internally controlled by calcite ($\delta^{13}C_{CO_2\text{-calcite}} \sim -10.4$ to -7.9 ‰ PDB) is consistent
510 with mixing between the CO₂ component internally controlled by calcite, and a second CO₂
511 component due to degradation of organic matter, whose $\delta^{13}C_{CO_2\text{-organic matter}}$ is assumed $\sim -$
512 25.5 ‰ PDB. From the $\delta^{13}C_{CO_2}$ of each clay sample, we estimate the contribution of these
513 components ($X_{\text{organic matter}}$ and X_{calcite}) in percent for the three boreholes (Figure 9). The profiles
514 of organic contribution are similar in the AUB1010 and AUB230 boreholes and provide
515 evidence that degradation of organic matter is the major source of CO₂ in calcite-free surficial
516 formations ($X_{\text{organic matter}} \sim 60$ -80%), at the top of the clay down to ~ 8 -9 m ($X_{\text{organic matter}} \sim 32$ -
517 60%), and toward the interface with Greensands ($X_{\text{organic matter}}$ up to 60 ‰). The depth of about
518 ten meters corresponds approximatively to the depth of the root network observed in
519 boreholes.

520 The contributions given in percent may be used to estimate the DIC associated to these
521 contributions:

522
$$\text{DIC}_{\text{calcite}} = X_{\text{calcite}} \times \text{DIC} \text{ and } \text{DIC}_{\text{organic matter}} = X_{\text{organic matter}} \times \text{DIC}$$

523

524 From the top of the clay to ~10 m for AUB230 and AUB1010, the $\text{DIC}_{\text{calcite}}$ increased from 1-2
525 to 6.5 mmol/L, and then decreased to ~1-2 mmol/L at 20-25 m for AUB 230 and at 16 m for
526 AUB1010. The $\text{DIC}_{\text{calcite}}$ in the weathered clay was higher than the average DIC value
527 measured in the reduced clay, which is attributed to calcite equilibrium in the reduced system
528 (1.5 ± 0.5 mmol/L PW referred to as $\text{DIC}_{\text{calcite } 0}$). That confirms the displacement of the

529 carbonate system ($\text{DIC}_{\text{calcite dissolution}}$) with pyrite oxidation and decreasing pH (Table 2).
530 According to the reaction (c), one mole of CO_2 and one mole of Ca are produced by
531 dissolution of one mole of CaCO_3 . The $\text{DIC}_{\text{calcite dissolution}}$ partially explains the Ca concentration
532 increase in pore waters, but Ca concentration is also controlled by Ca-bearing mineral
533 precipitation such as gypsum and the clay exchanger (Lerouge et al., 2018).

534 The $\text{DIC}_{\text{calcite dissolution}}$ also can be expressed in millimoles of dissolved calcite per 100 g of rock,
535 using the water and carbonate contents of the rock (Table 2). Even though CO_2 degassing
536 reveals the effects of weathering on the clay, the calculated percentages of calcite
537 dissolution to explain CO_2 degassing data remain small (<0.3 millimoles of calcite per 100 g
538 of rock) in the highly reactive transition zone. They are however higher in the weathered clay
539 from the AUB1010 than from the AUB230 borehole. That is consistent with a higher intensity
540 of clay weathering in the AUB1010 borehole, suggested by decreasing methane, and
541 increasing oxygen and nitrogen degassing. It is noteworthy that our calculations correspond
542 to a measurement at a time t of a reactive system, i.e. in situ reactivity and diffusion of pore
543 waters through the formation. The diffusion rate of oxygen dissolved in pore waters is so
544 slow that we assume minerals and the system were at a steady state (pseudo-equilibrium) at
545 a time t.

546 On the other side, at the bottom of the clay at ~34 m in the AUB1010 borehole and at ~68 m
547 in the AUB230, the DIC was lower than in preserved reduced Tégulines and $\delta^{13}\text{C}_{\text{CO}_2}$ was ~ -
548 18 ‰, suggesting a dilution or isotopic exchange of CO_2 internally controlled by calcite with
549 Greensands waters poor in CO_2 of organic origin. The profile of the $\delta^{13}\text{C}_{\text{CO}_2}$ in the lower part
550 of the clay suggests progressive diffusion of CO_2 of organic origin through the clay formation
551 up to ~ 30-40 m in the AUB230 borehole and ~20-25 m in the AUB1010 borehole.

552 Assuming contemporaneous weathering progressions at the top and the bottom of Tégulines
553 clay in the AUB230 and AUB1010 boreholes, the lower thickness of the clay formation in the
554 AUB1010 borehole and decompaction processes might explain the higher weathering
555 intensity in AUB1010 borehole.

556 **5.3. Modeling approach**

557 The distribution of DIC and major ions (Ca, Mg, Cl, SO_4^{2-}) with depth showed that the main
558 geochemical reactions occur in the soil zone (organic matter degradation), the highly reactive
559 and 0-10 m oxidized clay zone (pyrite oxidation and calcite dissolution), and in a lower
560 proportion at the interface with aquifer waters of underlying Greensands. The solute profiles
561 in the unoxidized clay are consequently the result of downward diffusion from pore waters of
562 the oxidized clay and of upward diffusion from aquifer waters of underlying Greensands.
563 Even though chloride is generally considered as a natural conservative tracer, chloride also
564 shows a curvilinear profile relatively well-correlated with DIC, Ca, Mg and SO_4^{2-} -profiles.
565 These ion concentrations combined with previous oxygen and hydrogen isotopes of clay
566 pore waters in the first ten meters of the AUB1010 borehole (Lerouge et al., 2018) seem to
567 support evaporation processes.

568 Since surface erosion rates are low in the Paris Basin (Prijac et al., 2000), we neglect
569 erosion processes and focus on chemical weathering. We now propose in a first approach to
570 simulate chemically in one dimension the DIC concentrations through the weathering profile
571 developed on Tégulines Clay, using the reactive transport code PhreeqC v3.1.2 (Parkhurst
572 and Appelo, 2013) with the ThermoChimie thermodynamic database (Giffaut et al., 2014).
573 The initial 1D-model setup considers a 32 meter high column (with 1 meter meshes) formed
574 of uniformly distributed reduced clay. The column height is approximatively the thickness of
575 the clay in the AUB1010 borehole. Initial porosity was 0.25 (Lerouge et al., 2018). Clay pore
576 waters chosen for the model were arbitrarily those of the AUB1010-23 m sample. Indeed,
577 Tégulines Clay is a marine formation, and consequently early pore waters had composition
578 close to seawater. However, the formation has been outcropped since ~23 Ma ago, and
579 meteoric waters have diffused through it since, and diluted the pore waters. The lack of
580 knowledge of the paleogeography and paleoclimate of the area do not allow a running
581 simulation over 23 Ma. In this study, we chose to model scenarios over a period of 10 kyrs,
582 which corresponds to the last ice age, even though the present-day pore-water chemistry is
583 not the same as 10 kyrs ago. Therefore, we assessed the pore waters by equilibration with
584 the calcite-pyrite-goethite- P_{CO_2} assemblage and the clay exchanger, according to the
585 THERMOAR model developed by (Gaucher et al., 2006; Gaucher et al., 2009). Since the
586 kinetic dissolution of silicate minerals such as quartz and feldspars is much longer than 10
587 kyrs (Appelo and Postma, 2005; Lasaga, 1984), we simplified the geochemical model
588 focusing on water-rock interactions of calcite and pyrite, and cation exchanges identified in
589 the weathered clay, and assumed silicate minerals to be stable. The surficial waters diffusing
590 through the vertical column considered in the model were natural pore waters in soil (TPH1-1

591 0-30 cm waters), equilibrated with the atmospheric pressure of oxygen, and taking into
592 account the kinetic reaction of organic matter degradation in soil (Marty et al., 2015; Marty et
593 al., 2018).

594 The diffusion coefficient was set to $5 \cdot 10^{-11}$ m²/s for each ion based on HTO experiments
595 (ANDRA, 2015). There was no consideration of multi-component diffusion (each ion with its
596 own diffusion coefficient; Hasenmueller et al., 2017).

597 In a first model, we considered the reactivity in soil and in the clay without evaporation. In
598 that case, the model did not reproduce the DIC curvilinear profile, with high DIC values in the
599 first meters, and ion curvilinear profiles (Figure 10). Different kinetics values for pyrite
600 oxidation and organic matter degradation did not significantly change the results.

601 In the second model, we introduced evaporation processes through concentrating surficial
602 waters by approximatively six-fold, and adjusted it to DIC measurements. In that way we
603 simulated evaporation processes in the first meter of the clay column (i.e. first cell of the
604 model). This second model reproduced the DIC curvilinear profile defined by core sample
605 degassing quite well and also alkalinities measured on pore waters extracted by squeezing
606 (Figure 10). This suggests that organic matter degradation in soil and evaporation processes
607 were the major reactions needed to explain the CO₂ anomaly in the 0-10 m zone of the
608 AUB1010 borehole, which is consistent with the CO₂ carbon isotope data, which also show
609 the major contribution of CO₂ derived from organic-matter degradation in soil into this zone.
610 Our model differs on this point from the Opalinus Clay chemical weathering model, where
611 kerogen in the clay formation is considered as the major source of degraded organic matter
612 (Hasenmueller et al., 2017).

613 Even though the PhreeqC reactive transport modeling at ~10 kyrs reproduced the DIC profile
614 well, the profiles of major ions did not fit so well. Especially chloride concentration was not
615 high enough. Further investigations need to be made in terms of knowledge of
616 paleogeography, hydrology of the system and timing of the processes to explain the
617 discrepancies between the reactive transport model and the data. For chloride and sulfate,
618 discrepancies might be due to some anionic exclusion considered as negligible in Tégulines
619 Clay (Lerouge et al., 2018) and/or to diffusion coefficients different for each ion, as has been
620 demonstrated for Opalinus Clay (Van Loon et al., 2018). In addition, the model does not
621 include how porosity changes with time or the complex water/gas behavior in the
622 unsaturated/saturated zone. Taking into account these parameters might partially solve
623 discrepancies between the model and the data. However, this is beyond the scope of this
624 study ; other reactive transport codes (CrunchFlow, TOUGHREACT, MIN3P (Bao et al.,
625 2017; Mayer et al., 2002), or HP1 (Jacques and Šimůnek, 2005; Jacques et al., 2008;
626 Šimůnek et al., 2006)) that have been developed to model such hydrogeochemical

627 processes (Li et al., 2017; Steefel et al., 2015) are more suitable for watershed scale
628 modeling.

629 **6. Conclusion**

630 In degassing claystone, monitoring CO₂, O₂, N₂ and alkane gas and carbon isotopes on CO₂
631 we have powerful techniques for defining the depth of the weathering profile in a reduced-
632 marine clay formation. These contribute to a better understanding of weathering processes.
633 In our case study of Tégulines Clay from the eastern part of the Paris Basin, degassed CO₂
634 significantly increased between 4 and 11 m in the highly reactive transition zone of the
635 weathering profile. The δ¹³C of degassed CO₂ provided evidence of the two major CO₂
636 sources: organic matter degradation and the calcite equilibrium. The increase of degassed
637 CO₂ corresponds both to the degradation of plant roots observed in borehole down to 11 m
638 and to calcite dissolution due to acidic pH (pyrite oxidation, organic matter degradation), due
639 to interactions with oxygen diffusing from atmosphere through the clay. The measurements
640 of CO₂ concentration in the gas phase relative to a volume of degassed clayrock allowed us
641 to estimate the equivalent concentrations of total CO₂ dissolved in clay pore waters that are
642 consistent with total dissolved-carbonate concentration and alkalinity values in clay pore
643 waters extracted by squeezing. Measurements of CO₂ and O₂ partial pressures of constitute
644 key parameters for accurately describing and understanding processes affecting pore water
645 chemistry in the highly reactive transition zone of the weathering profile. Coupled with DIC
646 modeling, those data revealed that evaporation is an additional key parameter to consider in
647 understanding the critical zone and the processes occurring at the redox front. Overall, our
648 results suggest that dissolved gases and their isotopic signatures are good markers of
649 weathering processes in the critical zone.

650 Acknowledgments

651 The French National Radioactive Waste Management Agency (ANDRA) and the French
652 Geological Survey (BRGM) supported this study through the GAULT_ZC project. We thank
653 the Associate Editor, Dr Thomas Gimmi, and two anonymous referees for their constructive
654 comments and significant improvements to the manuscript. We are grateful to Dr Karen M.
655 Tkaczyk (McMillan translation) for proofreading and editing the English text.
657

658 7. References

- 659 Aarão Reis, F.D.A., Brantley, S.L., 2019. The impact of depth-dependent water content on
660 steady state weathering and eroding systems. *Geochimica et Cosmochimica Acta* 244, 40-
661 55.
- 662 Amédéo, F., Matrimon, B., Magniez-Jannin, F., Touch, R., 2014. La limite Albien inférieur-
663 Albien moyen dans l'Albien type de l'Aube (France): ammonites, foraminifères, séquences.
664 *Revue de Paléobiologie* 33, 159-279.
- 665 ANDRA, 2015. PNGMDR 2013-2015 Projet de stockage de déchets radioactifs de faible
666 activité massique à vie longue (FA-VL) Rapport d'étape 2015.
667 <https://www.andra.fr/sites/default/files/2018-01/rapport-etape-favl.pdf>.
- 668 Appelo, C., Postma, D., 2005. *Geochemistry, groundwater and pollution*, CRC. Balkema,
669 Rotterdam.
- 670 Bolton, E.W., Berner, R.A., Petsch, S.T., 2006. The Weathering of Sedimentary Organic
671 Matter as a Control on Atmospheric O₂: II. Theoretical Modeling. *American Journal of*
672 *Science* 306, 575-615.
- 673 Brantley, S.L., Goldhaber, M.B., Ragnarsdottir, K.V., 2007. Crossing disciplines and scales to
674 understand the critical zone. *Elements* 3, 307-314.
- 675 Brantley, S.L., Holleran, M.E., Jin, L., Bazilevskaya, E., 2013. Probing deep weathering in the
676 Shale Hills Critical Zone Observatory, Pennsylvania (USA): the hypothesis of nested
677 chemical reaction fronts in the subsurface. *Earth Surface Processes and Landforms* 38,
678 1280-1298.
- 679 Debure, M., Tournassat, C., Lerouge, C., Madé, B., Robinet, J.-C., Fernández, A.M.,
680 Grangeon, S., 2018. Retention of arsenic, chromium and boron on an outcropping clay-rich
681 rock formation (the Tégulines Clay, eastern France). *Science of The Total Environment* 642,
682 216-229.
- 683 Deines, P., Langmuir, D., Harmon, R.S., 1974. Stable carbon isotope ratios and the
684 existence of a gas phase in the evolution of carbonate ground waters. *Geochimica et*
685 *Cosmochimica Acta* 38, 1147-1164.
- 686 Dideriksen, K., Christiansen, B.C., Baker, J.A., Frandsen, C., Balic-Zunic, T., Tullborg, E.,
687 Mørup, S., Stipp, S.L.S., 2007. Fe-oxide fracture fillings as a palæo-redox indicator:
688 Structure, crystal form and Fe isotope composition. *Chemical Geology* 244, 330-343.
- 689 Drake, H., Tullborg, E.-L., MacKenzie, A.B., 2009. Detecting the near-surface redox front in
690 crystalline bedrock using fracture mineral distribution, geochemistry and U-series
691 disequilibrium. *Applied Geochemistry* 24, 1023-1039.
- 692 Duffy, C., Shi, Y., Davis, K., Slingerland, R., Li, L., Sullivan, P.L., Goddérès, Y., Brantley, S.L.,
693 2014. Designing a Suite of Models to Explore Critical Zone Function. *Procedia Earth and*
694 *Planetary Science* 10, 7-15.
- 695 Fernández, A.M., Sánchez-Ledesma, D.M., Tournassat, C., Melón, A., Gaucher, E.C.,
696 Astudillo, J., Vinsot, A., 2014. Applying the squeezing technique to highly consolidated
697 clayrocks for pore water characterisation: Lessons learned from experiments at the Mont
698 Terri Rock Laboratory. *Applied Geochemistry* 49, 2-21.

- 699 Gaucher, É.C., Blanc, P., Bardot, F., Braibant, G., Buschaert, S., Crouzet, C., Gautier, A.,
700 Girard, J.-P., Jacquot, E., Lassin, A., Negrel, G., Tournassat, C., Vinsot, A., Altmann, S.,
701 2006. Modelling the porewater chemistry of the Callovian–Oxfordian formation at a regional
702 scale. *Comptes Rendus Geoscience* 338, 917-930.
- 703 Gaucher, E.C., Lassin, A., Lerouge, C., Fléhoc, C., Marty, N.C.M., Henry, B., Tournassat, C.,
704 Altmann, S., Vinsot, A., Buschaert, S., Matray, J.M., Leupin, O.X., De Craen, M., 2010. CO₂
705 partial pressure in clayrocks: a general model, *Water-Rock Interaction WRI-13*. Taylor &
706 Francis Group (CRC Press), Guanajuato, Mexico, pp. 855-858.
- 707 Gaucher, E.C., Tournassat, C., Pearson, F.J., Blanc, P., Crouzet, C., Lerouge, C., Altmann,
708 S., 2009. A robust model for pore-water chemistry of clayrock. *Geochimica et Cosmochimica*
709 *Acta* 73, 6470-6487.
- 710 Giffaut, E., Grivé, M., Blanc, P., Vieillard, P., Colàs, E., Gailhanou, H., Gaboreau, S., Marty,
711 N., Made, B., Duro, L., 2014. Andra thermodynamic database for performance assessment:
712 ThermoChimie. *Applied Geochemistry* 49, 225-236.
- 713 Girard, J.-P., Fléhoc, C., Gaucher, E., 2005. Stable isotope composition of CO₂ outgassed
714 from cores of argillites: a simple method to constrain $\delta^{18}\text{O}$ of porewater and $\delta^{13}\text{C}$ of
715 dissolved carbon in mudrocks. *Applied Geochemistry* 20, 713-725.
- 716 Graz, Y., 2009. Production and fate of fossil organic carbon released by mechanical and
717 chemical weathering of marly formations: Jurassic marls of Draix experimental watersheds,
718 France. Université d'Orléans.
- 719 Harmand, D., O, L., Jaillet, S., Allouc, J., Occhiotti, S., Brulhet, J., Fauvel, P., Hamelin, B.,
720 Laurain, M., Roux, J., Marre, A., Pons-Branchu, E., 2004. Dynamique de l'érosion dans le
721 Barrois et le Perthois (Est du Bassin de Paris) : incision et karstification dans les bassins-
722 versants de la Marne, de la Saulx et de l'Ornain. [Dynamics of erosion in the Barrois and the
723 Perthois regions (East of the Paris Basin) : incision and karstification in the watersheds of the
724 Marne, Saulx and Ornain rivers.]. *Quaternaire* 15, 305-318.
- 725 Hasenmueller, E.A., Gu, X., Weitzman, J.N., Adams, T.S., Stinchcomb, G.E., Eissenstat,
726 D.M., Drohan, P.J., Brantley, S.L., Kaye, J.P., 2017. Weathering of rock to regolith: The
727 activity of deep roots in bedrock fractures. *Geoderma* 300, 11-31.
- 728 Heidari, P., Li, L., Jin, L., Williams, J.Z., Brantley, S.L., 2017. A reactive transport model for
729 Marcellus shale weathering. *Geochimica et Cosmochimica Acta* 217, 421-440.
- 730 Hendry, M.J., Wassenaar, L.I., 2000. Controls on the distribution of major ions in pore waters
731 of a thick surficial aquitard. *Water Resour. Res.* 36, 503-513.
- 732 Jin, L., Brantley, S.L., 2011. Soil chemistry and shale weathering on a hillslope influenced by
733 convergent hydrologic flow regime at the Susquehanna/Shale Hills Critical Zone
734 Observatory. *Applied Geochemistry* 26, S51-S56.
- 735 Jin, L., Ravella, R., Ketchum, B., Bierman, P.R., Heaney, P., White, T., Brantley, S.L., 2010.
736 Mineral weathering and elemental transport during hillslope evolution at the
737 Susquehanna/Shale Hills Critical Zone Observatory. *Geochimica et Cosmochimica Acta* 74,
738 3669-3691.
- 739 Keller, C., 2019. Carbon Exports from Terrestrial Ecosystems: A Critical-Zone Framework.
740 *Ecosystems*.

- 741 Kim, H.-C., Lee, K., 2009. Significant contribution of dissolved organic matter to seawater
742 alkalinity.
- 743 Lasaga, A.C., 1984. Chemical kinetics of water-rock interactions. *Journal of geophysical*
744 *research: solid earth* 89, 4009-4025.
- 745 Lebedeva, M.I., Fletcher, R.C., Balashov, V.N., Brantley, S.L., 2007. A reactive diffusion
746 model describing transformation of bedrock to saprolite. *Chemical Geology* 244, 624-645.
- 747 Lerouge, C., Blessing, M., Flehoc, C., Gaucher, E.C., Henry, B., Lassin, A., Marty, N.,
748 Matray, J.M., Proust, E., Rufer, D., Tremosa, J., Vinsot, A., 2015. Dissolved CO₂ and Alkane
749 Gas in Clay Formations. *Procedia Earth and Planetary Science* 13, 88-91.
- 750 Lerouge, C., Claret, F., Tournassat, C., Grangeon, S., Gaboreau, S., Boyer, B., Borschnek,
751 D., Linard, Y., 2014. Constraints from sulfur isotopes on the origin of gypsum at
752 concrete/claystone interfaces. *Physics and Chemistry of the Earth, Parts A/B/C* 70–71, 84-
753 95.
- 754 Lerouge, C., Grangeon, S., Gaucher, E.C., Tournassat, C., Agrinier, P., Guerrot, C., Widory,
755 D., Fléhoc, C., Wille, G., Ramboz, C., Vinsot, A., Buschaert, S., 2011. Mineralogical and
756 isotopic record of biotic and abiotic diagenesis of the Callovian–Oxfordian clayey formation of
757 Bure (France). *Geochimica et Cosmochimica Acta* 75, 2633-2663.
- 758 Lerouge, C., Robinet, J.-C., Debure, M., Tournassat, C., Bouchet, A., Fernandez, A.M.,
759 Flehoc, C., Guerrot, C., Kars, M., Lagroix, F., Landrein, P., Madé, B., Negrel, P., Wille, G.,
760 Claret, F., 2018. A Deep Alteration and Oxidation Profile in a Shallow Clay Aquitard:
761 Example of the Tégulines Clay, East Paris Basin, France. *Geofluids* 2018, 20.
- 762 Li, L., Maher, K., Navarre-Sitchler, A., Druhan, J., Meile, C., Lawrence, C., Moore, J.,
763 Perdrial, J., Sullivan, P., Thompson, A., Jin, L., Bolton, E.W., Brantley, S.L., Dietrich, W.E.,
764 Mayer, K.U., Steefel, C.I., Valocchi, A., Zachara, J., Kocar, B., McIntosh, J., Tutolo, B.M.,
765 Kumar, M., Sonnenthal, E., Bao, C., Beisman, J., 2017. Expanding the role of reactive
766 transport models in critical zone processes. *Earth-Science Reviews* 165, 280-301.
- 767 Marty, N.C., Claret, F., Lassin, A., Tremosa, J., Blanc, P., Madé, B., Giffaut, E., Cochepin, B.,
768 Tournassat, C., 2015. A database of dissolution and precipitation rates for clay-rocks
769 minerals. *Applied Geochemistry* 55, 108-118.
- 770 Marty, N.C., Lach, A., Lerouge, C., Grangeon, S., Claret, F., Fauchet, C., Madé, B., Lundy,
771 M., Lagroix, F., Tournassat, C., 2018. Weathering of an argillaceous rock in the presence of
772 atmospheric conditions: A flow-through experiment and modelling study. *Applied*
773 *Geochemistry* 96, 252-263.
- 774 Mazurek, M., Alexander, W.R., MacKenzie, A.B., 1996. Contaminant retardation in fractured
775 shales: matrix diffusion and redox front entrapment. *Journal of contaminant hydrology* 21, 71-
776 84.
- 777 Mook, W.G., Bommerson, J.C., Staverman, W.H., 1974. Carbon isotope fractionation
778 between dissolved bicarbonate and gaseous carbon dioxide. *Earth and Planetary Science*
779 *Letters* 22, 169-176.
- 780 Parkhurst, D.L., Appelo, C.A.J., 2013. Description of Input and Examples for PHREEQC
781 Version 3—a Computer Program for Speciation, Batch-reaction, One-dimensional Transport,
782 and Inverse Geochemical Calculations.

- 783 Prijac, C., Doin, M.P., Gaulier, J.M., Guillocheau, F., 2000. Subsidence of the Paris Basin
784 and its bearing on the late Variscan lithosphere evolution: a comparison between Plate and
785 Chablis models. *Tectonophysics* 323, 1-38.
- 786 Schaap, M.G., Leij, F.J., Van Genuchten, M.T., 2001. Rosetta: A computer program for
787 estimating soil hydraulic parameters with hierarchical pedotransfer functions. *Journal of*
788 *hydrology* 251, 163-176.
- 789 Soulet, G., Hilton, R.G., Garnett, M.H., Dellinger, M., Croissant, T., Ogrič, M., Klotz, S.,
790 2018a. In situ measurement of flux and isotopic composition of CO₂ released during
791 oxidative weathering of sedimentary rocks. *Biogeosciences* 15, 4087-4102.
- 792 Soulet, G., Hilton, R.G., Garnett, M.H., Dellinger, M., Croissant, T., Ogrič, M., Klotz, S.,
793 2018b. Technical note: In situ measurement of flux and isotopic composition of CO₂ released
794 during oxidative weathering of sedimentary rocks. *Biogeosciences* 15, 4087-4102.
- 795 Steefel, C.I., Appelo, C.A.J., Arora, B., Jacques, D., Kalbacher, T., Kolditz, O., Lagneau, V.,
796 Lichtner, P.C., Mayer, K.U., Meeussen, J.C.L., Molins, S., Moulton, D., Shao, H., Šimůnek,
797 J., Spycher, N., Yabusaki, S.B., Yeh, G.T., 2015. Reactive transport codes for subsurface
798 environmental simulation. *Computational Geosciences* 19, 445-478.
- 799 Sullivan, P.L., Ma, L., West, N., Jin, L., Karwan, D.L., Noireaux, J., Steinhoefel, G., Gaines,
800 K.P., Eissenstat, D.M., Gaillardet, J., Derry, L.A., Meek, K., Hynek, S., Brantley, S.L., 2016.
801 CZ-tope at Susquehanna Shale Hills CZO: Synthesizing multiple isotope proxies to elucidate
802 Critical Zone processes across timescales in a temperate forested landscape. *Chemical*
803 *Geology* 445, 103-119.
- 804 Torres, M.A., West, A.J., Li, G., 2014. Sulphide oxidation and carbonate dissolution as a
805 source of CO₂ over geological timescales. *Nature* 507, 346-349.
- 806 Tostevin, R., Shields, G.A., Tarbuck, G.M., He, T., Clarkson, M.O., Wood, R.A., 2016.
807 Effective use of cerium anomalies as a redox proxy in carbonate-dominated marine settings.
808 *Chemical Geology* 438, 146-162.
- 809 Tremosa, J., Arcos, D., Matray, J.M., Bensenouci, F., Gaucher, E.C., Tournassat, C., Hadi,
810 J., 2012. Geochemical characterization and modelling of the Toarcian/Domerian porewater at
811 the Tournemire underground research laboratory. *Applied Geochemistry* 27, 1417-1431.
- 812 Tune, A., Druhan, J., Wang, J., Cargill, S., Murphy, C., Rempe, D., 2017. Linking carbon and
813 hydrologic fluxes in the critical zone: Observations from high-frequency monitoring of a
814 weathered bedrock vadose zone, AGU Fall Meeting Abstracts.
- 815 Tuttle, M.L.W., Breit, G.N., 2009. Weathering of the New Albany Shale, Kentucky, USA: I.
816 Weathering zones defined by mineralogy and major-element composition. *Applied*
817 *Geochemistry* 24, 1549-1564.
- 818 Tuttle, M.L.W., Breit, G.N., Goldhaber, M.B., 2009. Weathering of the New Albany Shale,
819 Kentucky: II. Redistribution of minor and trace elements. *Applied Geochemistry* 24, 1565-
820 1578.
- 821 Van Loon, L.R., Leupin, O.X., Cloet, V., 2018. The diffusion of SO₄²⁻ in Opalinus Clay:
822 Measurements of effective diffusion coefficients and evaluation of their importance in view of
823 microbial mediated reactions in the near field of radioactive waste repositories. *Applied*
824 *Geochemistry* 95, 19-24.

- 825 Wersin, P., Mazurek, M., Mäder, U.K., Gimmi, T., Rufner, D., Lerouge, C., Traber, D., 2016.
826 Constraining porewater chemistry in a 250 m thick argillaceous rock sequence. *Chemical*
827 *Geology* 434, 43-61.
- 828 White, T., Brantley, S., Banwart, S., Chorover, J., Dietrich, W., Derry, L., Lohse, K.,
829 Anderson, S., Aufdendkampe, A., Bales, R., Kumar, P., Richter, D., McDowell, B., 2015.
830 Chapter 2 - The Role of Critical Zone Observatories in Critical Zone Science, in: Giardino,
831 J.R., Houser, C. (Eds.), *Developments in Earth Surface Processes*. Elsevier, pp. 15-78.
- 832 Yesavage, T., Fantle, M.S., Vervoort, J., Mathur, R., Jin, L., Liermann, L.J., Brantley, S.L.,
833 2012. Fe cycling in the Shale Hills Critical Zone Observatory, Pennsylvania: An analysis of
834 biogeochemical weathering and Fe isotope fractionation. *Geochimica et Cosmochimica Acta*
835 99, 18-38.
- 836 Yu, C., Drake, H., Mathurin, F.A., Åström, M.E., 2017. Cerium sequestration and
837 accumulation in fractured crystalline bedrock: The role of Mn-Fe (hydr-)oxides and clay
838 minerals. *Geochimica et Cosmochimica Acta* 199, 370-389.
839
- 840
- 841
- 842

843 List of figures and tables

844 Figure 1: (a) Geological map of the eastern part of the Paris basin and location of the
845 studied area; (b) Location of the boreholes.

846 Figure 1: Lithological log of Tégulines clay based on the AUB111 and AUB121
847 boreholes (Lerouge et al., 2018), and major mineralogy of Tégulines clay from the
848 two boreholes AUB230 and AUB1010 and from the TPH1-1 pit with depth. The
849 brownish zones indicate the surficial zones in which the weathering processes
850 (reworked sediments/highly oxidized sediments) have significantly modified the bulk
851 rock mineralogy.

852 Figure 3: Micrographs of the thin sections of téguline clay from the AUB230 borehole
853 between 3.5 and 11.5 m in natural transmitted light providing evidence of the
854 presence of carbonate bioclasts and pyrite oxidation down to 10.30 m.

855 Figure 4: P_{CO_2} monitoring (mbar) of core samples from the AUB1010 borehole. (a)
856 gas-tight glass jars; (b) gas-leaking glass jars.

857 Figure 5: Schema of the core degassing dispositive including all the parameters that
858 are recorded.

859 X_i is the concentration (given in volume %) of the i species in the gas phase, P_{total} is the total gas
860 pressure, and V_G is the volume of gas in the glass jar. M and V_R are the mass (in g) and the volume (in
861 L) of rock in the glass jar. W is the water content of the rock (in weight %). $[i]_{(0)}$ and $[i]_{(t)}$ are the initial
862 and final concentrations of the species dissolved in pore waters (given in mmol/L), respectively. In
863 grey, the data that we measure and in red, the data we want to calculate.

864 Figure 6: Gas concentrations (CO_2 , CH_4 , O_2 and N_2) of samples from AUB1010,
865 AUB230 and AUB240 boreholes with depth. A schematic log is given for each
866 borehole to define the interfaces of Téguline Clay with surficial formations (loam) and
867 Greensands. Data are given in mmol/L of pore water. Black symbols represent
868 Tégulines Clay data, green symbols Brienne marl data and yellow symbols loam
869 data.

870 Figure 7: CO_2 Profiles with depth established for the three successive degassing of
871 core samples from the AUB1010 and AUB230 boreholes. A schematic log is given for
872 each borehole to define the interfaces of Téguline Clay with surficial formations
873 (loams) and Greensands. Data are given in mmol/L of pore water.

874 Figure 8: $\delta^{13}C_{CO_2}$ of samples from AUB1010, AUB230 and AUB240 boreholes with
875 depth. A schematic log is given for each borehole to define the interfaces of Téguline
876 Clay with surficial formations (loam) and Greensands. Data are given in δ permil
877 relative to the PDB standard. Black symbols represent Tégulines Clay data, green
878 symbols Brienne marl data and yellow symbols loam data.

879 Figure 9: Organic contribution (%) calculated on the base of a mixing between an
880 organic CO_2 endmember (-25 ‰ PDB) and a calcite equilibrium-derived CO_2
881 endmember (-7.7 ‰ PDB).

882

883 Figure 10: DIC profile of the AUB1010 borehole compared with reactive transport
884 model of DIC using Phreeqc. ETP: Evapotranspiration.

885 Table1: Chemical compositions of ground waters collected at 5.4 m in the TPH1-1 pit,
886 and pore waters extracted by squeezing on four core samples from the TPH1-1 pit
887 and of eleven samples from the AUB230 borehole. P were the successive pressure
888 of extraction applied during the squeezing of the core sample.

889

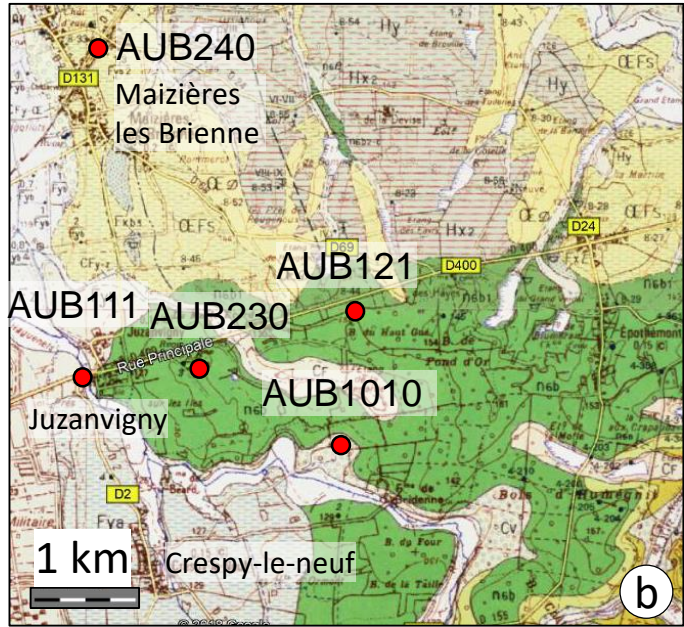
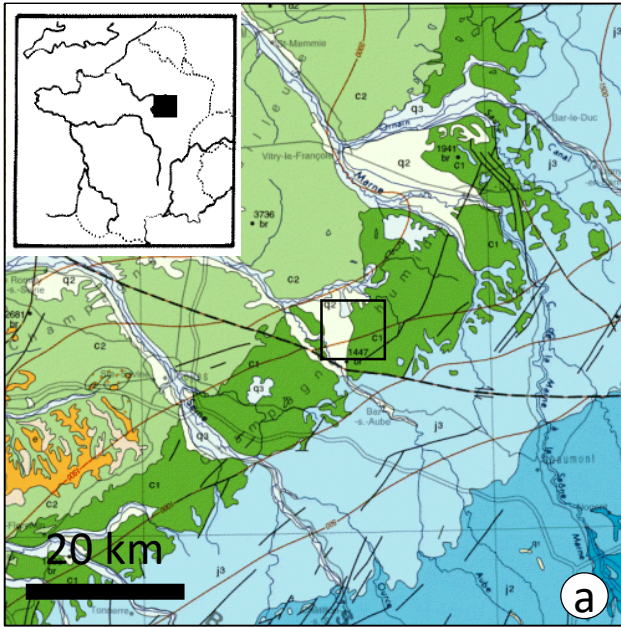
890 Table 2: AUB1010 and AUB230 boreholes - DIC, $\delta^{13}\text{C}_{\text{CO}_2}$, concentrations of CO_2
891 attributed to degradation of organic matter ($\text{DIC}_{\text{organic matter}}$), to total calcite ($\text{DIC}_{\text{calcite}}$)
892 calculated on the basis of a mixing between an organic CO_2 endmember (-27.4 ± 1.9
893 ‰ PDB) ($\text{DIC}_{\text{organic matter}}$) and a calcite equilibrium-derived CO_2 endmember ($-9.0 \pm$
894 1.3 ‰ PDB) and to calcite dissolution ($\text{DIC}_{\text{calcite dissolution}}$) calculated by $\text{DIC}_{\text{calcite}} -$
895 $\text{DIC}_{\text{calcite 0}}$ (1.5 ± 0.5 mmol/L PW), water content of the sample, conversion of $\text{DIC}_{\text{calcite}}$
896 dissolution in mmol/100 g of rock, calcite content of the sample and estimation of the
897 percent of calcite dissolution due to calcite system displacement.

898

899

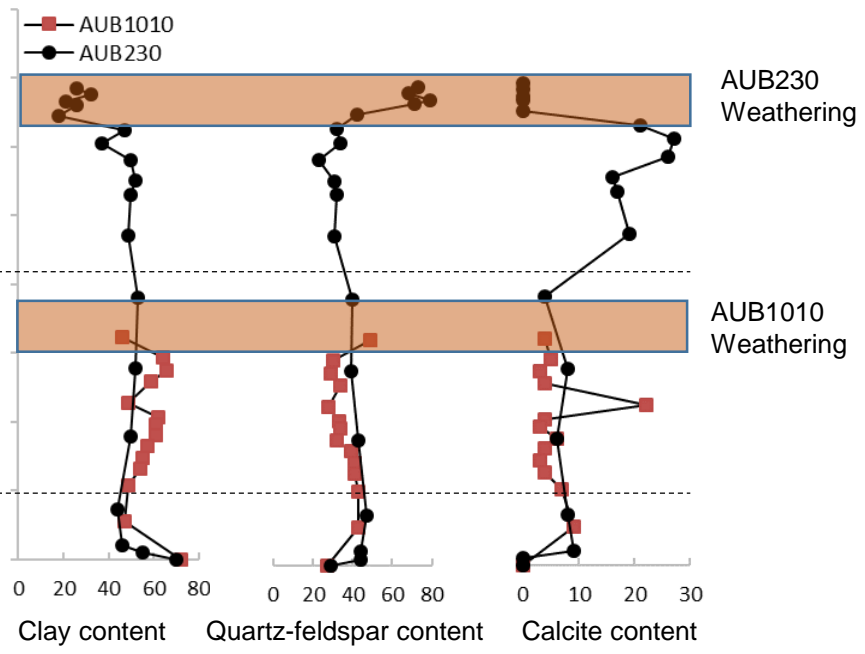
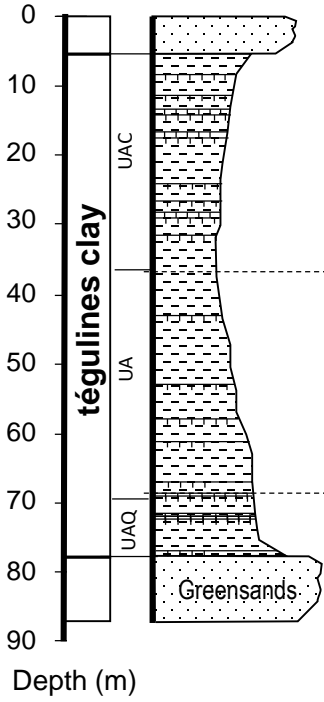
900

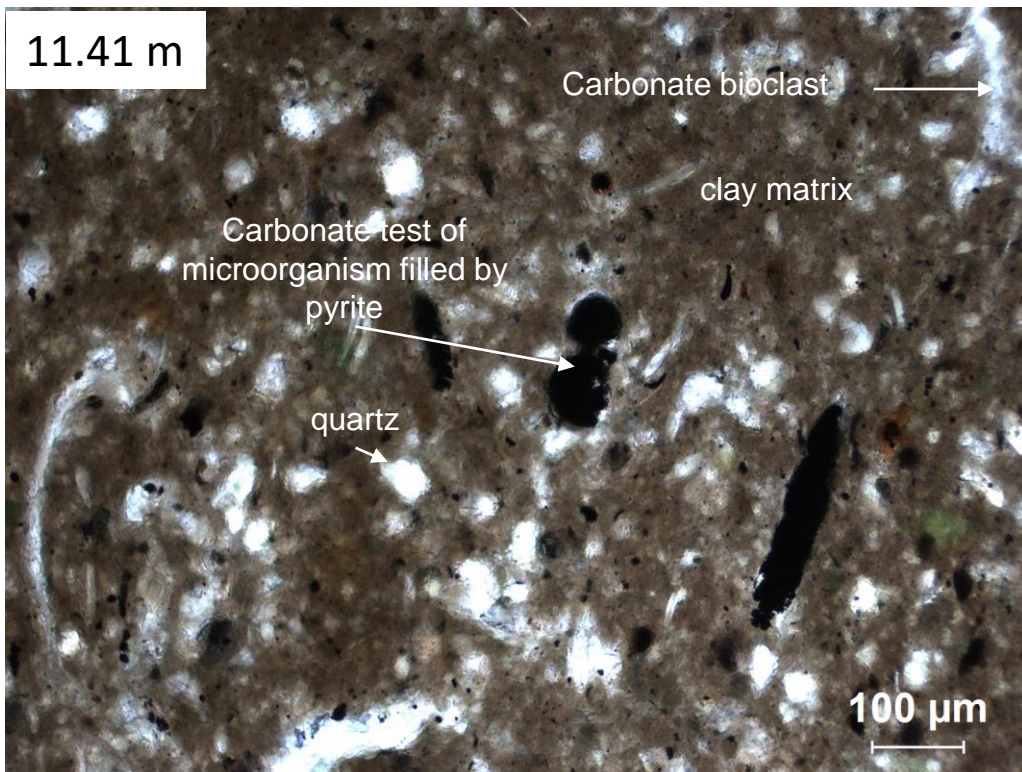
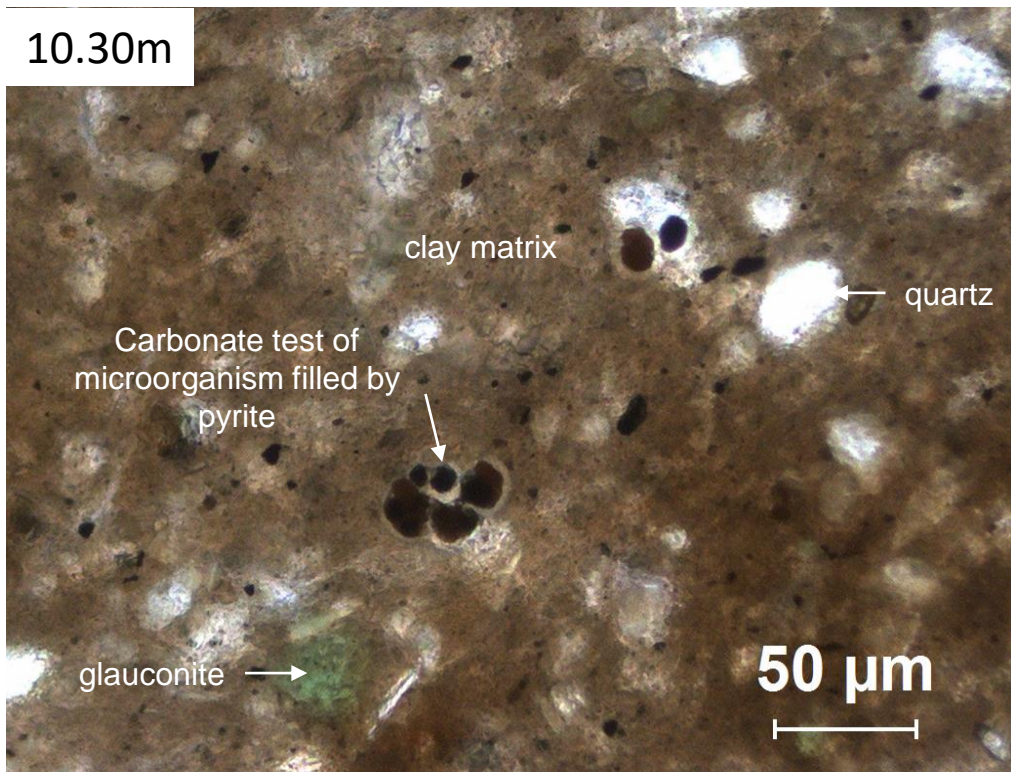
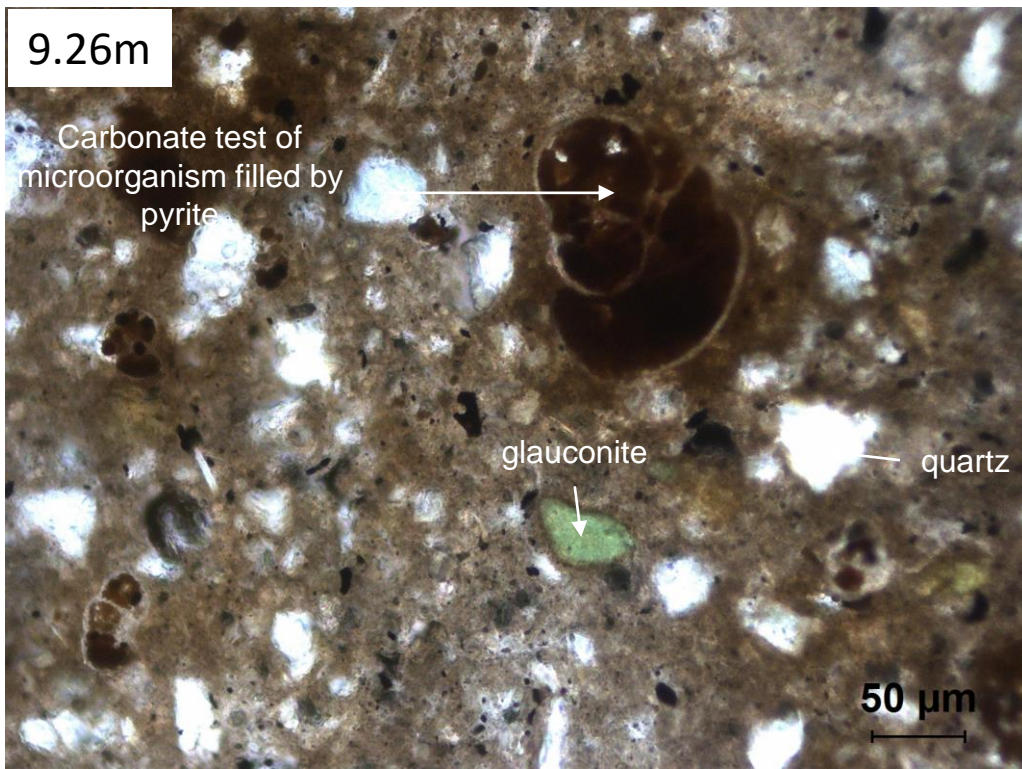
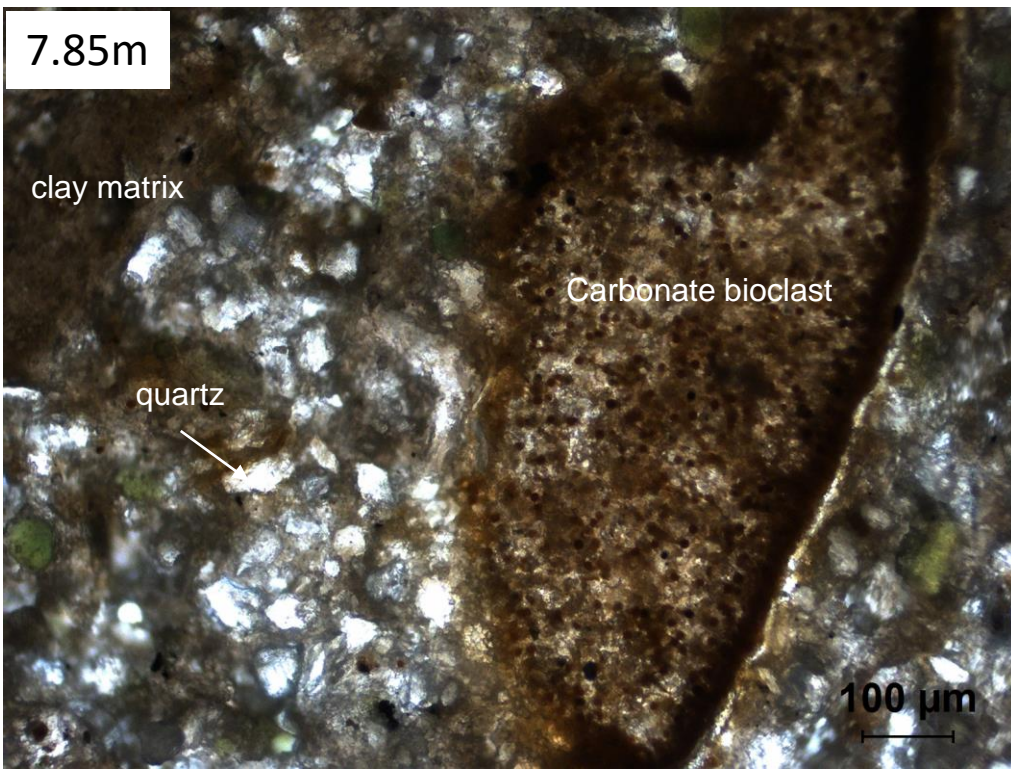
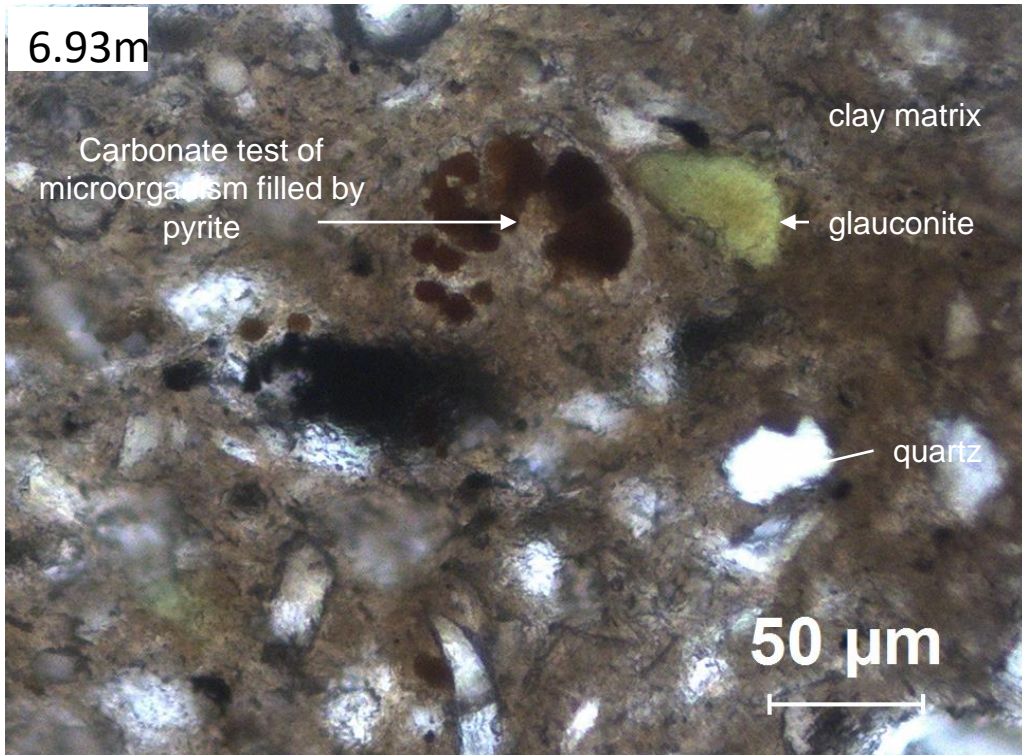
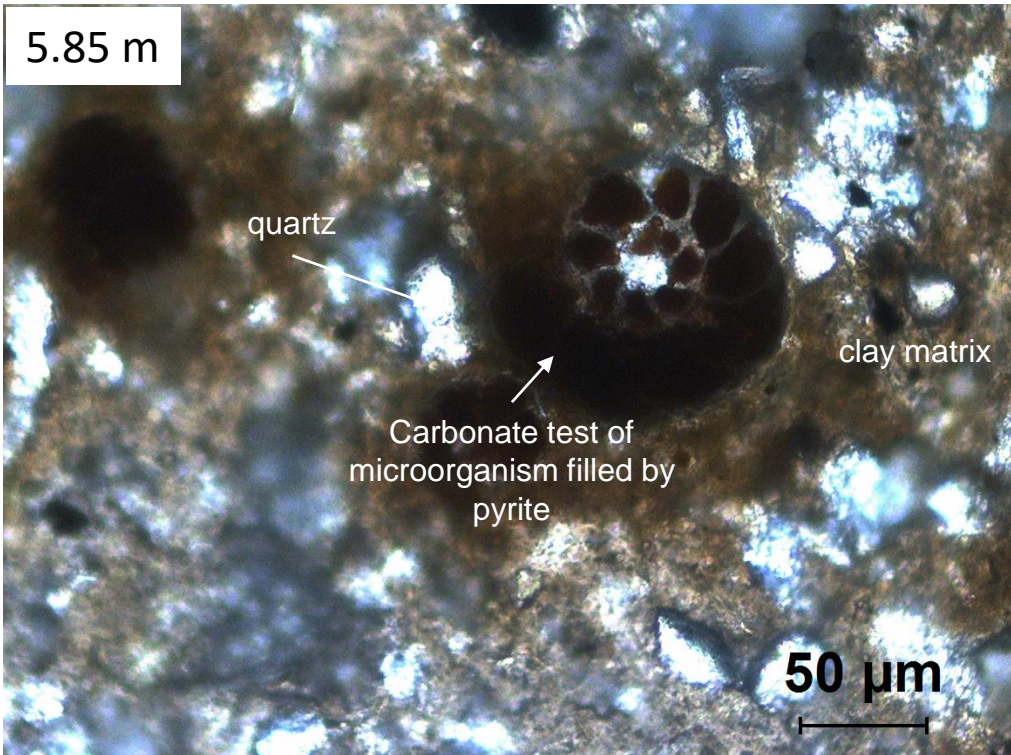
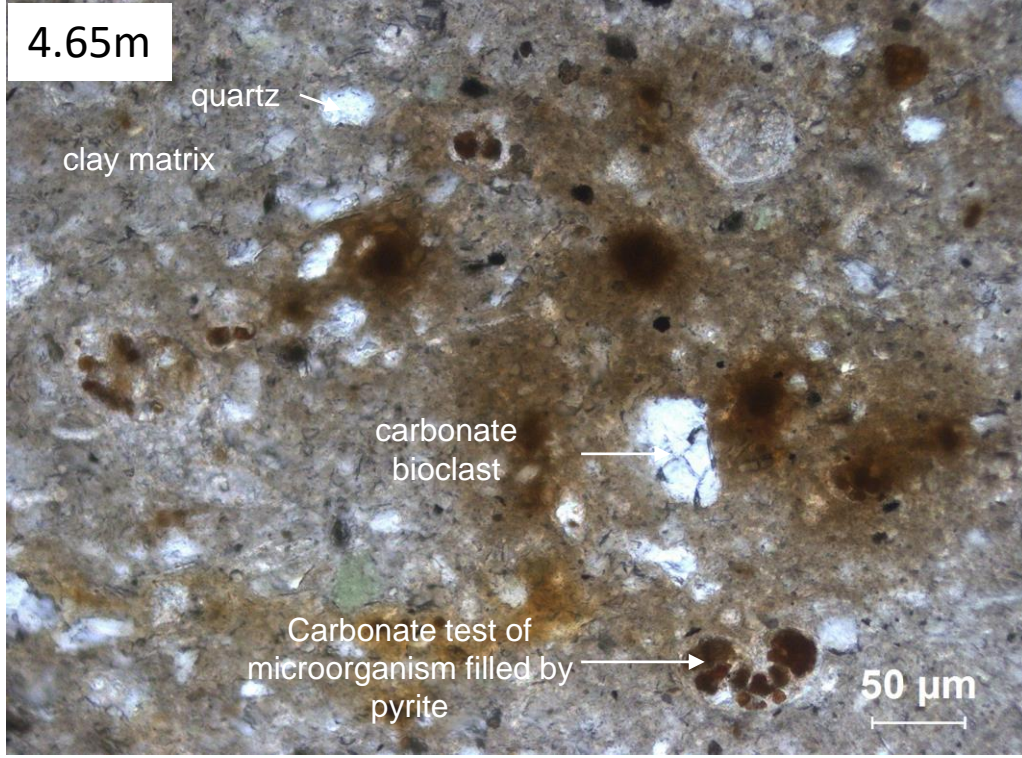
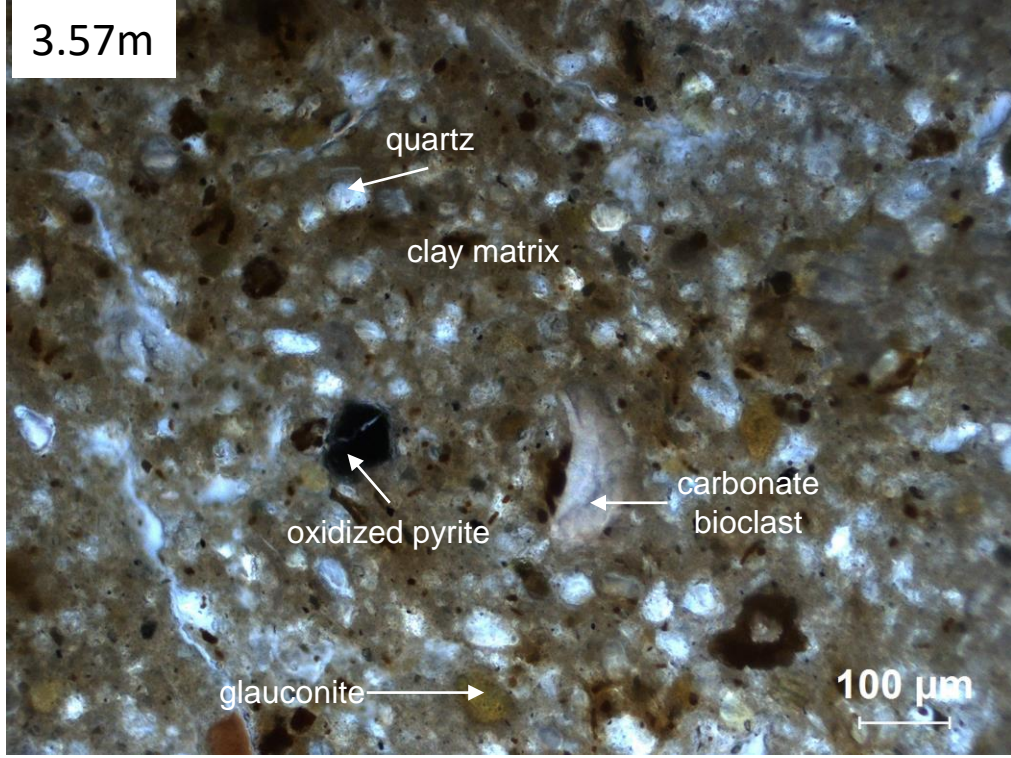
901



- | | | | |
|---|-----------------|---|------------------|
|  | Quaternary |  | Early Cretaceous |
|  | Eocene |  | Late Jurassic |
|  | Late Cretaceous |  | Middle Jurassic |

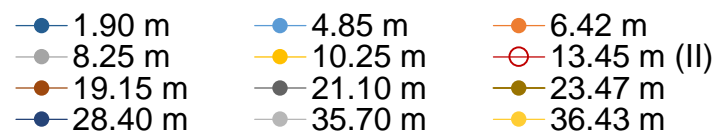
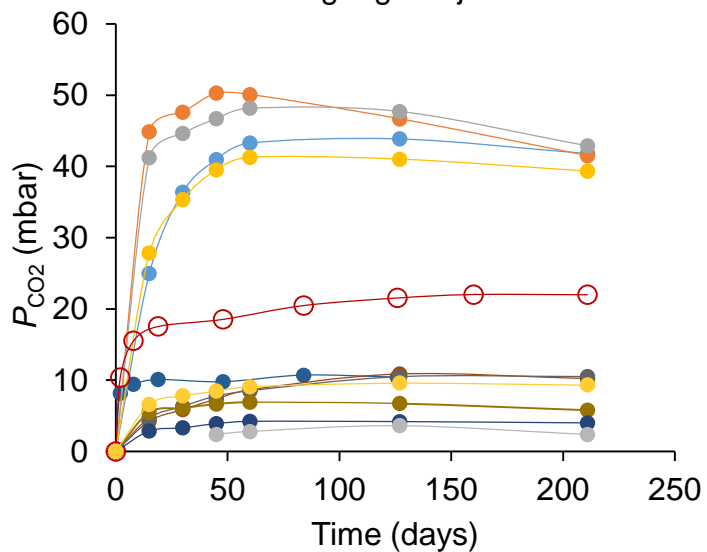
- | | | | |
|---|-----------------|---|------------|
|  | Tégulines Clay |  | Quaternary |
|  | Greensands | | |
|  | Plicatules Clay | | |



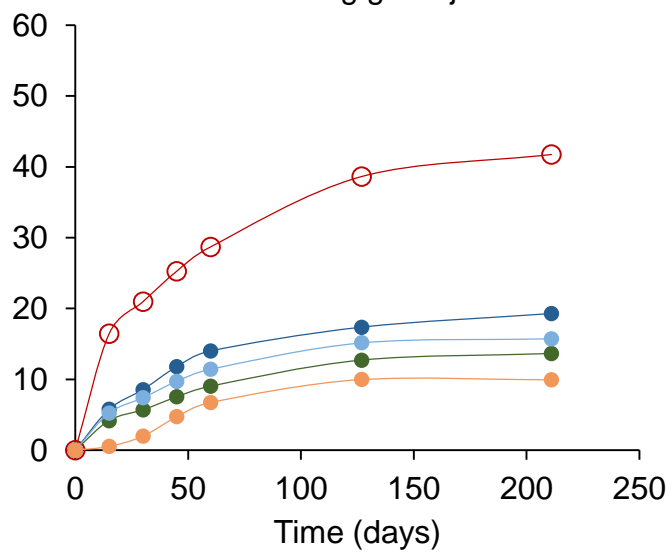


a

Gas-tight glass jars

**b**

Leaking glass jars



Gas

T, V_G

Initial state

$P_{\text{total}(0)}$

\approx

Final state

$P_{\text{total}(f)}$

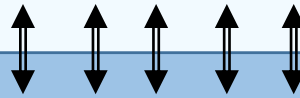
$X_{\text{CO}_2}, X_{\text{N}_2}, X_{\text{O}_2}$

$P_{\text{total}(0)}$

Water (W)

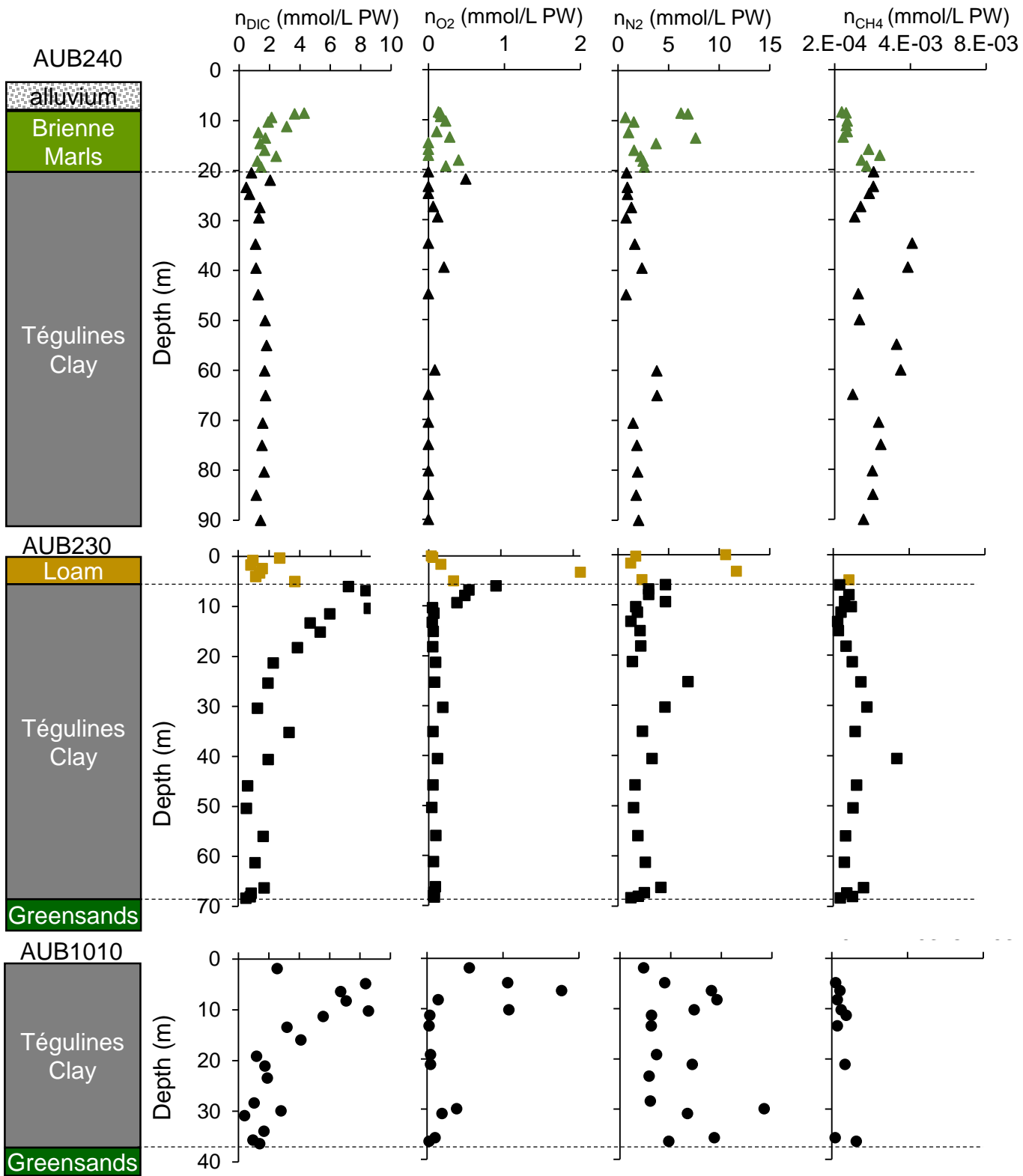
$[N_2]_{\text{aq}(0)}, [O_2]_{\text{aq}(0)},$
 $DIC_{(0)}, [CO_2]_{\text{aq}(0)},$
 $[HCO_3^-]_{(0)}, [CO_3^{2-}]_{(0)}$

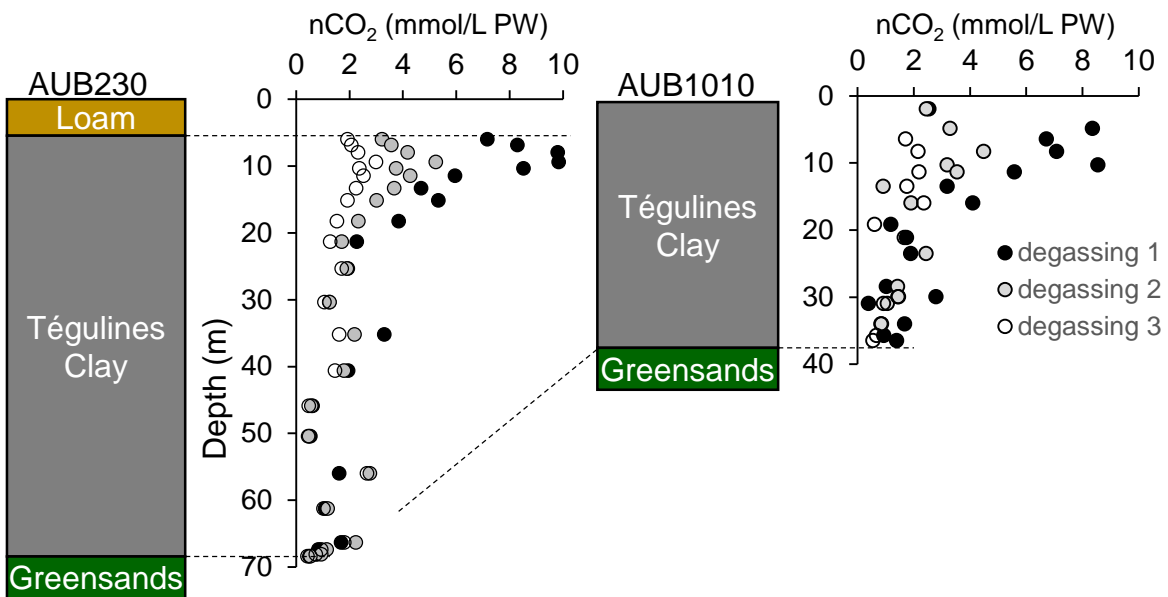
$[N_2]_{\text{aq}(f)}, [O_2]_{\text{aq}(f)},$
 $DIC_{(f)}, [CO_2]_{\text{aq}(f)},$
 $[HCO_3^-]_{(f)}, [CO_3^{2-}]_{(f)}$

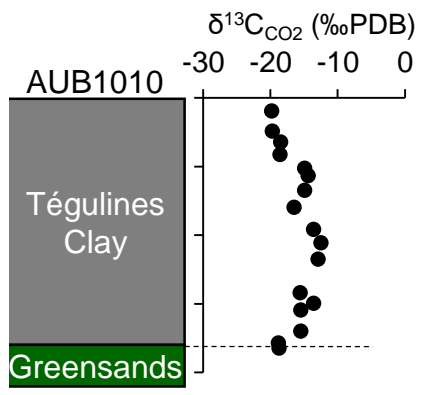
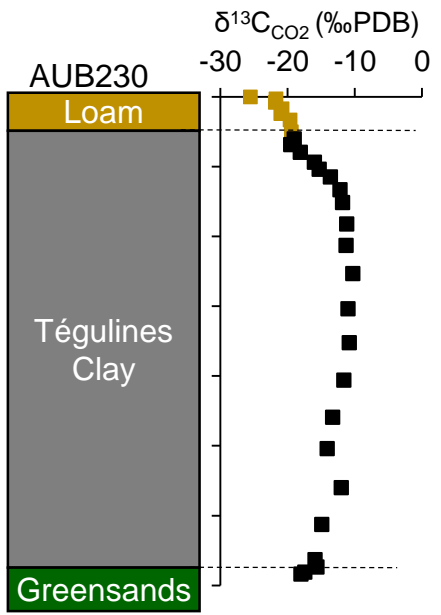
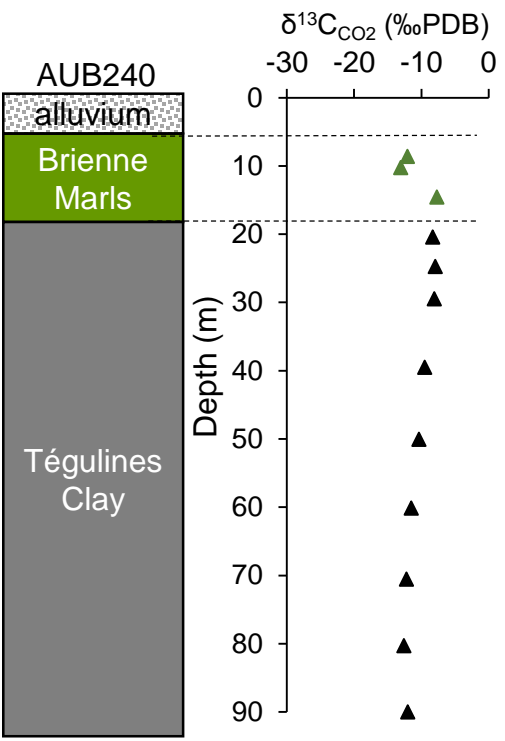


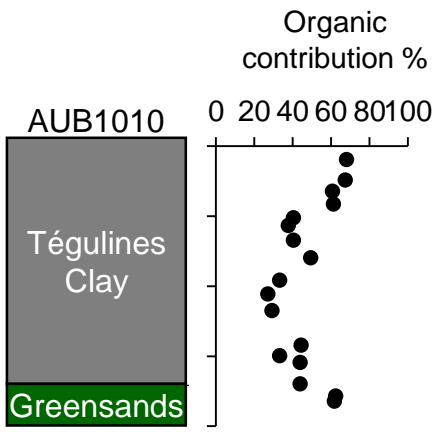
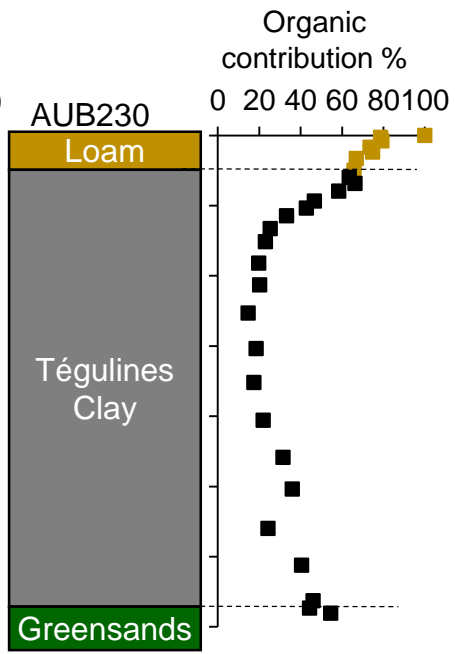
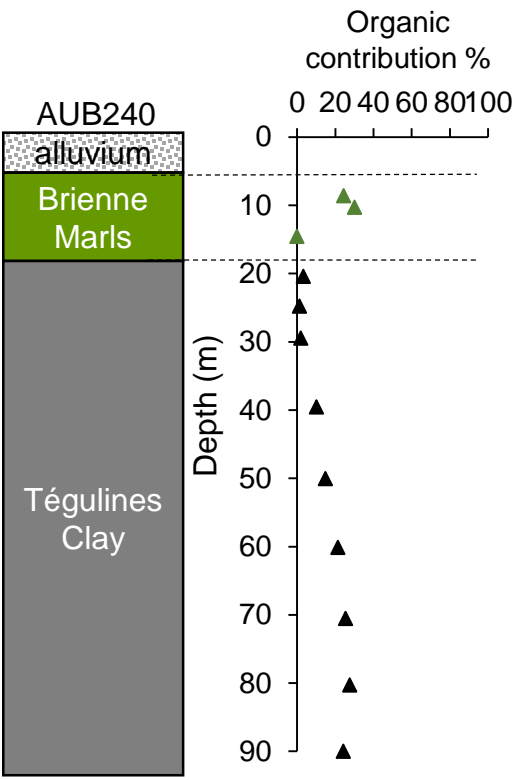
Clay rock

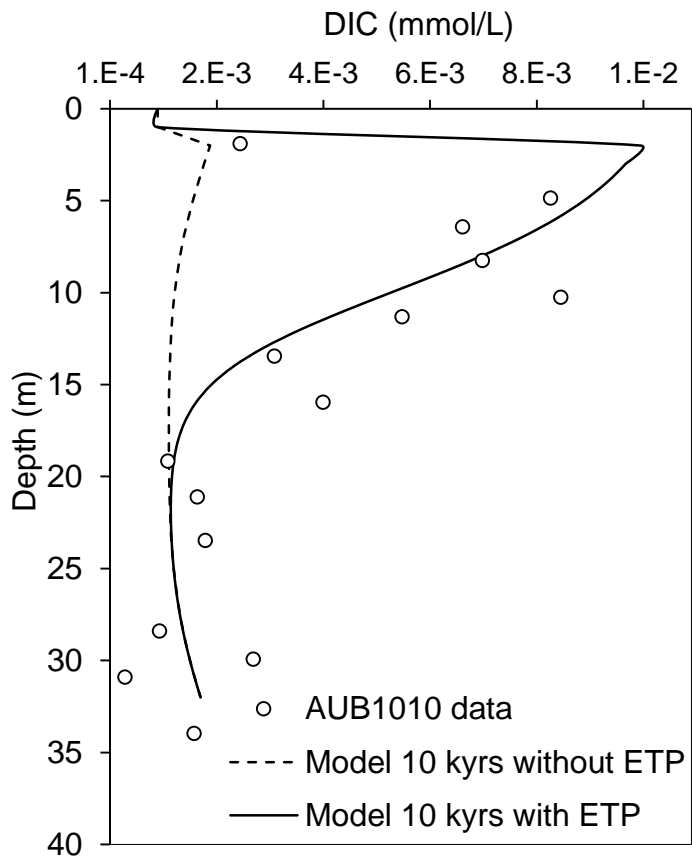
M, V_R











	TPH1-1 pit					AUB230 borehole										
Depth (m)	0.3	1.7	2.4	4	5.4	5.9	7.9	11.4	15	21	30.4	41	50	61.3	66.3	68.4
P (MPa)	5	5,10	10	5		5	15	15, 30	10, 15	15	10, 20	40, 60	40	50	50, 60	40
pH	7.2	7.0	6.8	7.2	7.4	7.5	7.4	7.8	7.4	7.5	8.0	7.5	8.1	8.1	7.9	7.9
Alkalinity (meq/L)	1.4	0.9	< 0.5	0.8		5.5	8.1	6.5	4.4	4.2	2.9	3.0	2.3	3.5	2.9	2.0
Cations (mmol/L)																
Na ⁺	0.4	0.9	0.9	0.6	0.6	5.4	8.5	7.0	3.9	3.3	2.6	2.8	2.2	2.1	4.3	1.6
K ⁺	0.03	0.03	0.04	0.04	0.02	0.4	3.3	0.8	0.7	0.7	0.6	0.4	0.3	0.2	0.6	0.2
Ca ²⁺	0.8	1.0	0.4	0.4	1.5	11.2	15.0	11.2	15.0	7.7	4.0	5.0	2.1	1.4	8.0	0.8
Mg ²⁺	0.2	0.4	0.2	0.1	0.2	4.9	8.0	7.0	9.9	6.8	3.9	4.5	1.5	1.3	7.8	0.7
Sr ²⁺				0.02		0.09	0.14	0.15	0.18	0.23	0.17	0.42	0.08	0.08	0.59	0.06
Al ³⁺				0.01												0.01
Si				0.24	0.23	0.43	0.57	0.27	0.16	0.17	0.21	0.20	0.17	0.15	0.18	0.13
Anions (mmol/L)																
Cl ⁻	0.2	0.7	0.9	0.5	0.4	7.8	12.6	14.8	12.7	6.8	2.8	1.5	2.0	1.9	1.1	1.1
SO ₄ ²⁻	0.3	0.5	0.1	0.1	0.2	9.8	18.7	15.6	20.8	12.5	5.4	8.7	2.1	1.4	15.6	1.0
NO ₃ ⁻	0.0	0.9	0.5		1.99		0.03				0.02		0.02	0.03		

	DIC	$\delta^{13}\text{C}$	DIC organic matter	DIC calcite	σ	DIC calcite dissolution	σ	water content	DIC calcite dissolution	Calcite content	calcite diss.
	mmol/L	‰	mmol/L			mmol/L		%	mmol/100g	mol/100g	%
AUB230											
0.0	65.7	-25.5	65.7	0.0	-	-		20.5	-	0.00	
0.3	3.1	-21.7	2.4	0.7	0.08	-		18.4	-	0.00	
0.8	1.1	-21.8	0.9	0.3	0.03	-		17.8	-	0.00	
1.7	0.9	-20.8	0.7	0.3	0.03	-		22.7	-	0.00	
2.4	1.8	-21.0	1.3	0.5	0.06	-		15.5	-	0.00	
3.3	1.6	-19.6	1.0	0.6	0.07	-		16.3	-	0.00	
5.0	4.2	-19.4	2.6	1.6	0.18	-		18.5	-	below dl	
6.0	8.3	-19.0	5.0	3.3	0.4	2.2	1.1	19.0	0.04	0.21	0.02
6.8	9.7	-19.5	6.1	3.5	0.4	2.5	1.2	18.2	0.05	0.21	0.02
8.0	10.9	-18.1	6.0	5.0	0.6	3.9	1.3	14.4	0.06	0.27	0.02
9.4	11.4	-16.0	4.8	6.6	0.8	5.0	1.3	18.5	0.09	0.27	0.03
10.4	9.9	-15.3	3.7	6.2	0.7	4.5	1.2	16.6	0.08	0.26	0.03
11.5	6.7	-13.6	1.8	4.9	0.6	3.4	0.9	16.5	0.06	0.26	0.02
13.3	5.3	-12.2	1.0	4.4	0.5	2.8	0.8	16.9	0.05	0.26	0.02
15.1	6.0	-11.8	1.0	5.0	0.6	3.5	0.9	15.9	0.06	0.26	0.02
18.2	4.3	-11.2	0.5	3.7	0.4	2.3	0.7	13.2	0.03	0.26	0.01
21.3	2.6	-11.3	0.3	2.2	0.3	0.9	0.6	15.6	0.01	0.26	0.01
25.3	2.2	-10.3	0.2	2.0	0.2	0.7	0.6	15.6	0.01	0.26	0.00
AUB1010											
1.9	2.6	-19.8	1.9	1.0	0.1	0.4	0.4	18.9	0.01	0.05	0.01
4.9	8.8	-19.7	6.3	3.5	0.4	2.6	1.3	24.0	0.06	0.05	0.12
6.4	8.1	-18.5	4.6	3.5	0.4	2.8	1.2	23.0	0.06	0.03	0.22
8.3	8.0	-18.6	4.9	3.6	0.4	2.7	1.2	19.6	0.05	0.04	0.13
10.3	9.0	-14.9	3.5	6.4	0.7	5.0	1.2	17.6	0.09	0.06	0.15
11.3	5.6	-14.4	2.1	4.5	0.5	2.8	1.0	18.6	0.05	0.04	0.13
13.5	3.2	-14.9	1.4	2.5	0.3	1.1	0.8	23.5	0.03	0.03	0.08
16.0	2.5	-16.5	2.1	2.6	0.3	0.5	0.5	16.5	0.01	0.06	0.02
19.2	1.2	-13.6	0.4	1.1	0.1	0.2	0.2	20.1	0.00	0.03	0.01
21.1	1.7	-12.5	0.4	1.7	0.2	0.5	0.5	15.5	0.01	0.04	0.02